PhysioPatch: A Multi-Modal Wearable Device for Continuous Cardiovascular and Cardiopulmonary Monitoring

by

Yusuf Ziya Hayırlıoğlu

A Dissertation Submitted to the
Graduate School of Sciences and Engineering
in Partial Fulfillment of the Requirements for
the Degree of

Master of Science

in

Electrical and Electronics Engineering

KOÇ ÜNİVERSİTESİ

December 8, 2023

PhysioPatch: A Multi-Modal Wearable Device for Continuous Cardiovascular and Cardiopulmonary Monitoring

Koç University

Graduate School of Sciences and Engineering

This is to certify that I have examined this copy of a master's thesis by

Yusuf Ziya Hayırlıoğlu

and have found that it is complete and satisfactory in all respects,

and that any and all revisions required by the final

examining committee have been made.

Committee Members:

Assist. Prof. Beren Semiz Gürsoy (Advisor)

Assist. Prof. Mehmet Cengiz Onbaşlı

Assist. Prof. Onur Ergen

Date:

To my family and friends, especially to my loving mother for her continuous support, and my brother for always standing up for me, this thesis is dedicated to you.

ABSTRACT

PhysioPatch: A Multi-Modal Wearable Device for Continuous Cardiovascular and Cardiopulmonary Monitoring
Yusuf Ziya Hayırlıoğlu
Master of Science in Electrical and Electronics Engineering
December 8, 2023

Remote monitoring systems offer significant advantages in assessing cardiovascular and cardiopulmonary health, facilitating early diagnosis and enabling personalized treatment plans. In this thesis, we present a novel wearable patch, *PhysioPatch*, which could facilitate comprehensive monitoring of cardiovascular and cardiopulmonary functions by simultaneously capturing various physiological signals, including electrocardiogram (ECG), seismocardiogram (SCG), photoplethysmogram (PPG), and body temperature. The design comprises a main body intended for placement on the mid-sternum and a detachable daughter body, enabling distal measurements to enhance comprehensive assessment. While the main body includes the sensors for measuring the body temperature, ECG, proximal PPG and SCG signals, and other electronics such as the microcontroller, the battery, the battery management system (BMS), the Bluetooth, and the microSD card; the daughter body houses the sensors for distal PPG and SCG signal acquisition. Along with the system design, the algorithms to derive various hemodynamic parameters (heart rate (HR), heart rate variability (HRV), respiration rate, oxygen saturation (SpO_2), and blood pressure (BP)) are also presented. The system was validated with a human subject study including 20 participants, and the results have revealed that the *PhysioPatch* is capable of achieving high-quality signals, resulting in accurate derivation of hemodynamic parameters. Overall, such a system could potentially offer continuous health monitoring outside clinical settings, regardless of time and environmental stressors.

ÖZETÇE

Physiopatch: Sürekli ve Non-Invasif Kardiyovasküler ve Kardiyopulmoner Takip İçin Çoklu-Modlu Giyilebilir Cihaz
Yusuf Ziya Hayırlıoğlu
Elektrik ve Elektronik Mühendisliği, Yüksek Lisans
8 Aralık 2023

Uzaktan izleme sistemleri, kardiyovasküler ve kardiyopulmoner sağlığı değerlendirmekte önemli avantajlar sunmakta, erken teşhisi kolaylaştırmakta ve kişiye özel tedavi planlarını mümkün kılmaktadır. Bu tezde, *PhysioPatch* adlı yeni bir giyilebilir cihazı sunmaktayız; bu cihaz, elektrokardiyogram (ECG), sismokardiyogram (SCG), fotopletismogram (PPG) ve vücut sıcaklığı dahil olmak üzere çeşitli fizyolojik sinyalleri eş zamanlı olarak yakalayarak kardiyovasküler ve kardiyopulmoner fonksiyonların kapsamlı izlenmesini kolaylaştırır. Tasarım, sternum üzerine yerleştirilmek üzere bir ana gövde ve daha kapsamlı bir değerlendirmeyi sağlamak adına distal ölçümleri mümkün kılan bir çıkarılabilir ek gövde içerir. Ana gövde, vücut sıcaklığı, ECG, proksimal PPG ve SCG sinyallerini ölçen sensörlerle beraber mikrodenetleyici, pil, pil yönetim sistemi (BMS), Bluetooth ve microSD kart gibi elektronikleri içerir. Ek gövde ise, distal PPG ve SCG sinyali için gereken sensörleri içermektedir. Çeşitli hemodinamik parametreleri (kalp atış hızı (HR), kalp atış hızı değişkenliği (HRV), solunum hızı, oksijen saturasyonu (SpO_2) ve kan basıncı (BP)) hesaplamayı sağlayan algoritmalar da bu tezde sunulmaktadır. Sistem, 20 katılımcıyı içeren bir insan deneyi çalışmasıyla doğrulanmış ve sonuçlar, *PhysioPatch*'in yüksek kaliteli sinyaller elde edebildiğini ve doğru hemodinamik parametre hesaplamalarına olanak tanıdığını göstermiştir. Genel olarak, bu tür bir sistem, zaman ve çevresel stres faktörlerinden bağımsız olarak klinik ortamların dışında sürekli sağlık kontrolü imkanı sunabilir.

ACKNOWLEDGMENTS

I would like to express my deepest respect and gratitude to my advisor Assist. Prof. Beren Semiz Gürsoy, for her endless support and efforts during my Master's journey. The completion of this thesis would not have been possible without her guidance.

I also would like to thank Assist. Prof. Mehmet Cengiz Onbaşlı, and Assist. Prof Onur Ergen for accepting to be in the thesis jury and for their previous mentorship during my academic journey.

I would like to thank Olgar Birsel, M.D for his guidance in clinical matters, and for his positive attitude that lifted my spirit up even when facing the tightest of deadlines.

A debt of gratitude is also owed to my friends in the lab for being there for me and creating a friendly atmosphere, especially Ali Najjar Amiri, for his advices and enjoyable conversations. I express my gratitude to all the people who volunteered in data collection process as well.

Last but not least, I would like to thank Hilal Demirtaş for their great help in administrative matters.

TABLE OF CONTENTS

LIST OF TABLES

LIST OF FIGURES

ABBREVIATIONS

ADC	Analog-to-Digital Converter
AO	Aortic Valve Opening
BMS	Battery Management System
BP	Blood Pressure
BPM	Beats Per Minute
CAD	Coronary Artery Disease
CNN	Convolutional Neural Network
DBP	Diastolic Blood Pressure
ECG	Electrocardiogram
EMG	Electromyogram
FIR	Finite Impulse Response
HASL	Hot Air Solder Leveling
HR	Heart Rate
HRV	Heart Rate Variability
Hb	Deoxygenated Hemoglobin
HbO_2	Oxygenated Hemoglobin
I2C	Inter-Integrated Circuit
IC	Integrated Circuit
IVC	Isovolumetric Contraction
LED	Light-Emitting Diode
LSTM	Long Short-Term Memory Network
Li-Po	Lithium-Polymer
MAE	Mean Absolute Error
MAPE	Mean Absolute Percentage Error
MC	Mitral Valve Closure
MSE	Mean Square Error
PAT	Pulse Arrival Time
PCB	Printed Circuit Board
PPG	Photoplethysmogram
PTT	Pulse-Transit Time
RMSE	Root Mean Square Error
RNN	Recurrent Neural Network
RTC	Real-Time Clock
SBP	Systolic Blood Pressure
SCG	Seismocardiogram
SVR	Support Vector Regression
SpO_2	Oxygen Saturation
UART	Universal Asynchronous Receiver/Transmitter

Chapter 1

INTRODUCTION

As per the 2020 World Health Organization report, cardiovascular and respiratory diseases stand as prominent contributors to global mortality, comprising a substantial portion of the overall recorded deaths internationally (∼30%) [WHO, 2020]. Furthermore, the Hospital Readmissions Reduction Program (2010), enacted as part of the Affordable Care Act, identified heart failure, acute myocardial infarction, and pneumonia as the primary health issues that require attention to lower rates of hospital readmissions [Zuckerman et al., 2016]. Given these findings, the implementation of remote and continuous monitoring systems holds the potential to facilitate early detection and intervention, create personalized treatment plans, and offer proactive and preventive care strategies for individuals susceptible to cardiovascular and cardiopulmonary diseases [Sana et al., 2020].

Primary clinical methods for diagnosis and monitoring involve evaluating (i) vital signs (blood pressure, heart rhythm, respiratory rhythm, and body temperature), (ii) chest and lung sounds, (iii) heart sounds, and (iv) vascular health [Gupta and Shea, 2021]. Therefore, there is a significant demand for innovative sensing methods and analytical processes to digitize these examination procedures, enabling continuous health monitoring independent of time and environmental stressors.

As electrical, mechanical, acoustic, and optical signals obtained from the human body originate from physiological processes, they offer valuable clinical insights into underlying anatomical and physiological conditions. Of these signals, the most frequently employed ones include the electrocardiogram (ECG), seismocardiogram (SCG), and photoplethysmogram (PPG) waveforms.

The electrocardiogram (ECG) furnishes details about the heart's electrical activity and is captured using electrodes affixed to the body surface. It comprises three key components: the P-wave, QRS complex, and T-wave. The P-wave corresponds to atrial depolarization, the QRS complex to ventricular depolarization, and the T-wave to ventricular repolarization [Odinaka et al., 2012]. Each segment between consecutive R-peaks in ECG signals corresponds to one heartbeat and typically varies between 600-1000ms. After calculating the average R-R interval ($\mathrm{RR}_{\mathrm{avg}}$), the average heart rate in terms of beats per minute can be obtained by $60/\mathrm{RR}_{\mathrm{avg}}$. The analysis of ECG signal plays a crucial role in evaluating various heart conditions, including coronary artery disease (CAD), arrhythmias, and cardiomyopathy.

While the ECG signal provides information about the electrical function of the heart, the SCG signal plays a crucial role in the mechanical assessment of the heart. The SCG is the measurement of chest vibrations that occur during the contraction of the heart and the pumping of blood into the vascular network [Inan et al., 2014]. It was first observed in 1992 that the SCG signal helps improve the diagnostic capability of the exercise stress test [Salerno et al., 1992]. Subsequent studies have also shown improved diagnosis results when SCG is used in conjunction with the ECG signal for CAD diagnosis compared to using only the ECG signal [Wilson et al., 1993]. Nowadays, SCG signals can be easily recorded through accelerometers. When three-axis accelerometers are used, these vibrations can be measured in the three fundamental planes of the body (Figure 1.1(a)), with each axis exhibiting a unique shape and pattern. The peaks in the SCG signal are directly related to underlying physiological events such as mitral valve closure (MC), isovolumetric contraction (IVC), aortic valve opening (AO), etc. While many studies in the literature have focused on the analysis of signals recorded in the dorsoventral axis [Taebi et al., 2019], recent studies have shown that signals in all three directions carry physiologically significant information. In fact, signals in the lateral and vertical planes may contain more information than the dorsoventral signal at times [Semiz et al., 2020]. Additionally, studies in the literature have demonstrated that SCG signal analysis can provide valuable clinical information without the need for invasive methods in various aspects, including systolic time intervals [Shandhi et al., 2019], assessment of myocardial contraction [Tavakolian et al., 2012], classification of heart failure [Inan et al., 2018], derivation of hemodynamic parameters such as stroke volume and heart rate [Semiz et al., 2020, Wahlström et al., 2017]. Taking all these studies into account, the development of a wearable device enabling the recording and analysis of SCG signals could bring comprehensive cardiovascular assessment to home environments, allowing continuous monitoring of individuals at risk of diseases and timely intervention in deteriorating health conditions.

The SCG signal primarily consists of two main components. The low-frequency (<20 Hz) portion arises from cardiac output, while the high-frequency (>20 Hz) portion, also known as the phonocardiogram, is generated in response to heart sounds [Castiglioni et al., 2007, Pandia et al., 2012]. Therefore, when recorded from the correct position, the SCG signal enables the evaluation of the heart both in terms of vibration and acoustics. The usefulness of the SCG signal is not limited to assessing cardiac health alone. The SCG signal also aids in detecting chest movements that occur due to the contraction and relaxation of the lungs during breathing. Studies in the literature have shown that the SCG signal can provide important clinical information when used to assess respiratory rhythm [Pandia et al., 2012], respiratory phases [Zakeri et al., 2016], and sleep apnea [Morillo et al., 2009]. Furthermore, pathological changes in the lungs (such as edema formation, bronchial obstruction, etc.) can alter the environmental and vibrational characteristics, leading to noticeable changes in the SCG signal [Dellacà et al., 2008]. Therefore, we believe that the diagnosis and monitoring of various lung pathologies can be possible through the SCG signal.

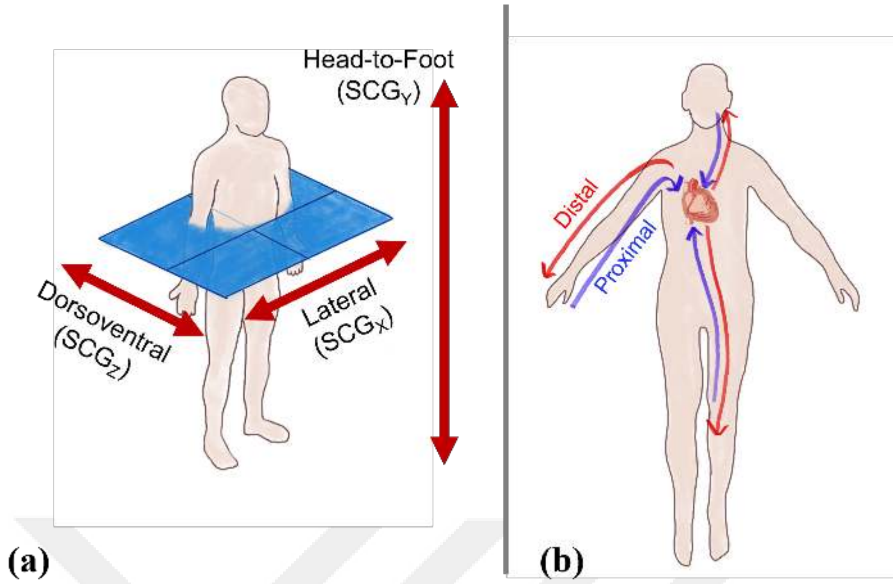

Figure 1.1: (a) The axes of the human body. (b) Regions defined as distal and proximal with respect to the heart.

In addition to the SCG signal, signals obtained from optical sensors can also be used for cardiopulmonary assessment. PPG is a type of signal that is widely used today and forms the basis for pulse oximeters, which measure blood oxygen levels. The working principle is based on an optical detection system consisting of a light source and a photodetector and is commonly used in many smartwatches and fitness trackers [Carek et al., 2017]. The volume of arterial blood throughout the cardiac cycle changes, and subsequently the amount of light absorbed in the arteries varies. The PPG signal is formed by measuring the reflected or transmitted light from the relevant region, depending on the operating mode of the photodetector [Elgendi, 2012]. In systems operating in reflection mode, the wavelength of light affects the penetration depth [Maeda et al., 2011]. Heart rate monitors used in smartwatches and activity bands often use green light sources over red or infrared light sources. Although green light allows for a high amplitude signal and reduces sensitivity to motion artifacts, its shorter wavelength only enables the assessment of the microvascular network on the skin surface [Lee et al., 2013, Maeda et al., 2011]. On the other hand, red and infrared lights with longer wavelengths can penetrate deeper into the tissue where the arteries are located, making them the optimal choices for vascular health and pulse wave timing studies. In literature, the analysis of the PPG signal has been shown to provide important information about blood oxygen levels, blood pressure, and vascular resistance [cheol Jeong et al., 2018].

In addition to the aforementioned signals, body temperature is one of the four fundamental vital signs (blood pressure, heart rate, respiratory rate, body temperature). Therefore, it has significant importance in cardiopulmonary and cardiovascular assessments. Particularly in infection conditions such as endocarditis (inflammation of the inner lining of the heart), fever is an inevitable symptom [Menni et al., 2020]. Hence, in addition to real-time physiological signals, regular monitoring of body temperature can play a crucial role in the diagnosis and monitoring of many diseases outside the hospital environment.

While various wearable system prototypes incorporating individual signals such as ECG, SCG, and PPG can be found in the literature [Fattah et al., 2017, Li et al., 2017, Di Rienzo et al., 2011, Hernandez et al., 2014, Da He et al., 2011], they have typically been restricted to heart rhythm assessment. As a result, none of these systems permits thorough monitoring of both cardiovascular and cardiopulmonary functions. Conversely, systems facilitating multiple measurements only facilitate signal recording from the specific location where the device is attached, thus lacking mobility functionality [Etemadi et al., 2015]. Given the anticipated scope of assessing lung health, respiratory function, and blood pressure parameters, the development of an adaptable and mobile system becomes imperative. Furthermore, it is crucial to create a system that supports real-time data transfer, facilitating prompt intervention when necessary.

We present a novel wearable patch, *PhysioPatch*, which could facilitate (i) comprehensive monitoring of cardiovascular and cardiopulmonary functions by simultaneously capturing various physiological signals (including ECG, SCG, PPG, and body temperature). The design comprises a main body intended for placement on the mid-sternum and a detachable daughter body, enabling distal SCG and PPG measurements for assessment of lungs and carotid arteries as well as the derivation of pulse arrival time (PAT) and BP values. The proposed system (ii) facilitates real-time data transfer and SD card recording while being (iii) adaptable and conducive to further development. Along with the system design, the algorithms to derive various hemodynamic parameters are also presented. The system was validated with a human subject study including 20 participants, and the results have revealed that the *PhysioPatch* is capable of achieving high-quality signals resulting in accurate derivation of hemodynamic parameters; hence, such a system could potentially offer continuous health monitoring outside clinical settings, regardless of time and environmental stressors.

Chapter 2

LITERATURE REVIEW

Most devices in the literature generally focused on heart rate monitoring. The ZioPatch, designed in a patch form, is based on a single-channel ECG principle and can be used for up to 14 days without the need for charging [Barrett et al., 2014]. After 14 days, users send the device to the analysis center by mail, and the recorded data is evaluated and reported to healthcare professionals. While the ZioPatch is based on offline analysis, the NUVANT MCT system, also designed in a patch form [Engel et al., 2012], allows recordings of single-channel ECG to the monitoring center directly, but the user cannot access their data and analysis live. Another product based on the single-channel ECG principle is the Kardia Mobile system, designed in the form of a phone case, providing users with accessible ECG signals within 30 seconds [Lau et al., 2013]. In addition to single-channel ECG systems, 12-channel ECG systems have also been developed. For example, the cvrPhone system sends the ECG recorded from 10 electrodes to a smartphone via Bluetooth [Sohn et al., 2017]. However, attaching numerous electrodes to various positions on the body is inconvenient for user usage and comfort.

Another approach used in monitoring heart rhythm and arrhythmias is the design of systems based on optical principles. One of the optical approaches presented in the literature involves the development of pulse monitoring systems using light-emitting diodes (LEDs) in phones [McManus et al., 2013]. However, data collection with such a system, the data is only collected when the user is placing their finger on the camera, making it impractical for continuous recording of signals throughout daily life. Additionally, the variability among phone models will affect signal quality. Another commonly used optical method, as introduced in the previous section, is the PPG signal. Various systems have been developed in the literature and the market based on the PPG signal. For example, the Scanadu Scout, is a portable device in a disc shape that records the user's PPG signal when held against the forehead [Walsh III et al., 2014].

However, similar to systems using phone LEDs, to continuously record signals throughout daily life with the Scout device is not feasible due to the requirement of placing it against the forehead. One of the most significant problems arising from this situation is that these systems do not allow patient monitoring during sleep. Attempts have been made to address this issue with devices designed in a watch format [Bai et al., 2018]. Activity tracking devices such as Apple Watch and Fitbit rely on green LED-based PPG signal analysis. Systems with sequentially arranged LEDs in different colors have also been developed, with two notable examples being the Wrist-Card designed in the form of a pulse oximeter [Fattah et al., 2017] and a vest-shaped tracking system [Li et al., 2017]. However, the most significant drawback of all these devices is that they primarily focus on heart rate monitoring and are unable to simultaneously record different physiological signals. Therefore, none of these systems is suitable for versatile cardiopulmonary assessment.

In addition to these products, wearable devices that allow the recording of different physiological signals in various forms have also been developed. One of the most important signals used in these systems is the SCG signal, recorded by accelerometers, introduced in the previous chapter. The contact of accelerometers with the body can be facilitated through adhesive tapes, plastic protectors, or textile products [Inan et al., 2014]. Currently, various wearable devices in different forms are available both in the literature and the market. One of the first wearable device prototypes developed for use outside the laboratory is the MagIC system, designed in the form of a vest, allowing the recording of both ECG and SCG signals [Di Rienzo et al., 2011]. Another notable system is designed in the form of a hearing aid, allowing the measurement of cardiogenic vibrations from within the ear [Da He et al., 2011]. In addition to these works, there are also studies suggesting the use of signals recorded through Google Glass sensors (three-axis accelerometer and three-axis gyroscope) for pulse and respiration monitoring (e.g., BioGlass by [Hernandez et al., 2014]). The studies presented by [Da He et al., 2011] and [Hernandez et al., 2014] have two significant drawbacks. First, the accuracy and sensitivity of these devices for cardiopulmonary assessment are open to question since vibration signals are recorded from a distant area from the chest. Second issue is the discomfort caused by the visibility of the devices in noticeable areas (such as the eyes and ears) during daily use.

Chapter 3

MATERIALS AND METHODS

There is a need for a system that enables real-time and comprehensive cardiovascular and cardiopulmonary monitoring outside hospital environments. Therefore, within this work, a wearable device that allows continuous cardiovascular monitoring, emphasizing developability and user convenience has been designed. The development of the device and the surrounding software can be divided into the following steps: (i) sensor selection, (ii) embedded software development, (iii) printed circuit board (PCB) design, (iv) case design, (v) human subject trials, and (vi) development of preliminary analysis algorithms.

One of the most important considerations in providing versatile cardiovascular and cardiopulmonary monitoring is from which positions physiological signals should be recorded. To meet clinical monitoring standards, the recorded signals must align with the examination steps used in clinical environments. Most devices in the literature enable the recording of signals only from the position where the device is attached and do not provide any mobility function. While using a single position (e.g., placing the device on the sternum) for evaluating parameters related only to the heart may not pose a problem, the device developed in this project has mobility and can assess lung health, respiration, and blood pressure parameters simultaneously. The adaptability of the device is a prominent feature for providing versatile cardiovascular and cardiopulmonary monitoring.

In clinical practice, the assessment of the lung and respiratory system is based on listening to multiple points on the chest and the back through a stethoscope. Therefore, devices directly placed on the chest or worn on the wrist in a watch format cannot be used for properly monitoring respiratory health. Furthermore, to obtain accurate information about blood pressure from the PPG signal, it is crucial to calculate pulse-transit time (PTT). Since PTT calculation requires two independent pulse wave measurements, one distal and one proximal (Figure 2c), systems where the PPG signal is recorded from a single point do not allow for the calculation of PTT. Therefore, there is a need for simultaneously recorded physiological signals from different points. Taking these into consideration, the *PhysioPatch* system consists of two parts: a main body mounted on the chest and a daughter body for distal measurements (Figure 3.1(b)). The device can be used either without the mobile body or with the mobile body attached. As seen in Figure 3.1(b-e), the mobile body could potentially enable the assessment of lungs and carotid arteries as well as the derivation of pulse arrival time and blood pressure values by leveraging distal SCG and PPG recordings. The details about the selected sensors are presented in the following subsections.

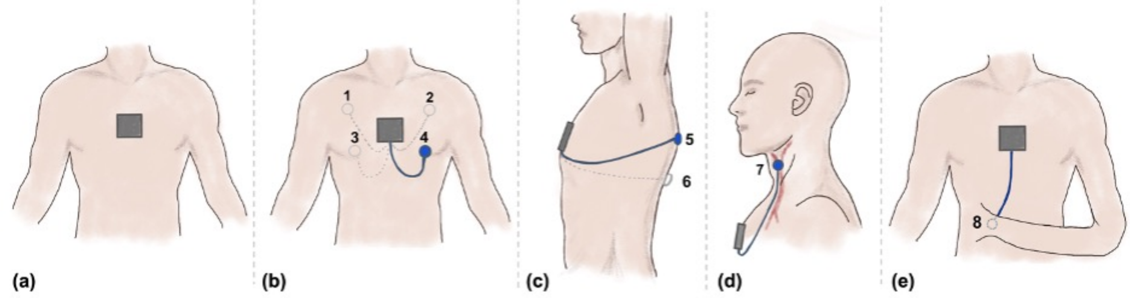

Figure 3.1: (a) The main body of the proposed wearable device was designed in such a way that ECG, SCG, PPG and body temperature measurements could be taken continuously. (b-e) The removable daughter body is designed to allow additional SCG and PPG measurements to assist in the analysis.

3.1 System Critical Components and Sensor Selection

3.1.1 Seismocardiogram (SCG) and Photoplethysmogram (PPG)

In the literature, the SCG signal has been analyzed using the frequencies below 100 Hz, and empirical evidence has shown that having a sample rate around 500 Hz is adequate [Semiz et al., 2020]. Despite analog accelerometers possessing a higher bandwidth in comparison to their digital counterparts, our aim was to select an accelerometer with high resolution, low noise, and sensitivity to achieve the measurement of peak-to-peak amplitude values within the <10 mg limits. Consequently, we chose the ADXL355 (Analog Devices, Norwood, MA, USA) accelerometer. It provides measurements with $25\mu g/\sqrt{Hz}$ noise floor and 0.003 mV/bit resolution, which has been proven successful in previous studies [Ganti et al., 2020]. Two ADXL355 accelerometers were included in the development kit - one for the main (chest) body and another one for the daughter body (Figure 3.2(b) and (e)).

For the PPG sensor, commercially available systems were examined. The majority of smartwatches on the market leverages the green light-emitting diodes (LEDs), as green LEDs have relatively higher signal quality and are less affected by the motion artifacts compared to infrared and red LEDs. However, green LED-based systems are limited to assessing the microvascular network on the skin's surface due to the relatively shorter wavelength of green light. In contrast, red and infrared LEDs possess longer wavelengths, enabling their penetration into deeper tissue layers where arteries are located [Lee et al., 2013, Maeda et al., 2011]. For that reason, the use of red and infrared LEDs was preferred in the development kit design. We decided on using a digital MAX30102 (Maxim Integrated, Sunnyvale, CA, USA) sensor with a sampling rate of 3200 samples/second and a resolution of 0.05 mV/bit. Two MAX30102 sensors were used in the design, one for the main body and another one for the daughter body (Figure 3.2(b) and (e)). As the MAX30102 only has one inter-integrated circuit (I2C) address; an I2C multiplexer, TCA9548A (Texas Instruments, Dallas, TX, USA), was used to enable communication on the same I2C bus when utilizing two of them.

While both the ADXL355 and MAX30102 sensors support I2C communication, it's important to note that the ADXL355 has a maximum clock frequency of 3.4 MHz, whereas the MAX30102 supports up to 400 kHz. Consequently, the I2C protocol's maximum clock frequency is capped at 400 kHz when utilizing the same signal bus. This speed was deemed sufficient for the system's requirements. Additionally, the ADXL355 operates at 3.3 V without on-board regulators, while the microcontroller's digital bus functions at 5 V. To prevent potential sensor damage, logic level enhancement mode field-effect transistors (BSS138 from ON Semiconductor Corporation, Phoenix, Arizona, USA) were employed for logic level shifting. Both the ADXL355 and MAX30102 sensor packages incorporate built-in FIFO buffers, allowing temporary on-sensor storage of data.

3.1.2 Electrocardiogram (ECG) and Body Temperature

To capture the ECG signal, we opted for the AD8232 analog front-end integrated circuit (IC) from Analog Devices, based in Norwood, MA, USA. This IC features a noise floor of 100 nV/$\sqrt{Hz}$, a gain of 100, and a gain-bandwidth product of 100 kHz (Figure 3.2(f)). Three gel electrodes were positioned in the Einthoven's triangle configuration, and the signals collected through these electrodes were processed using the AD8232. The resulting signal was subsequently sampled at a 10-bit resolution and a rate of 500 Hz utilizing the analog-to-digital converter (ADC) of the ATMEGA2560.

For body temperature measurement, LM35 (Texas Instruments, Dallas, TX, USA) analog IC with ±0.5°C accuracy, 10 mV/°C linear scale factor, -55°C - 150°C measurement range and 600 nV/$\sqrt{Hz}$ noise floor was chosen and integrated into the part to be mounted on the chest (Figure 3.2(b)). The signal was sampled by the ATMEGA2560's ADC at 10-bit resolution and 1 Hz.

3.1.3 Microcontroller

The criteria taken into account for the selection of the microcontroller were the following: having adequate processing power to enable data acquisition at the predetermined sampling rates; low active mode power consumption; large flash memory, SRAM and EEPROM area; high number of analog and digital pins for custom functionality; hardware interrupts and timers. Equipped with 256 kB of Flash memory, 8 kB SRAM, 4 kB EEPROM, 16 analog pins, and 86 programmable input/output lines, as well as four 16-bit timers and six hardware interrupts, ATMEGA2560 was our preference. In active mode powered with 5 V at 16 MHz clock via an external crystal oscillator, it has a current consumption of 20 mA. In low-power modes, it has a current consumption as low as 0.1 uA.

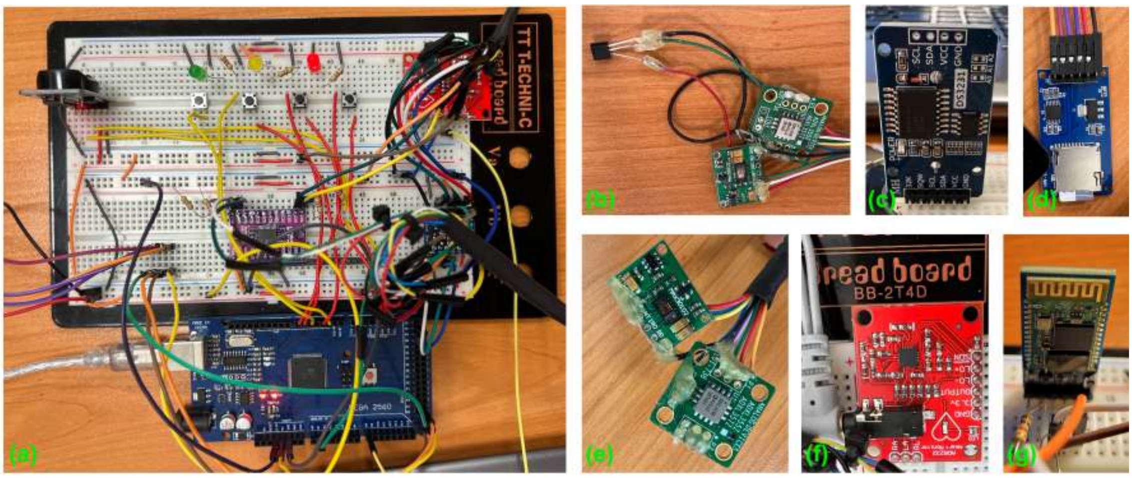

Figure 3.2: (a) General view of the system, (b) Temperature, MAX30102 and ADXL355 sensors to be mounted on the chest area, (c) DS3231 RTC module, (d) HW-125 microSD card module, (e) MAX30102 and ADXL355 sensors to be mounted on the wrist area, (f) AD8232 analog front-end IC, (g) HC-05 Bluetooth module

3.1.4 Data Storage and Transfer

To facilitate real-time data transfer, the development kit was equipped with Bluetooth functionality. In tandem with the Bluetooth connection, data was concurrently stored on a microSD card to serve as a backup. To ensure swift operation, a high write speed was sought for the SD card, leading to the selection of a 16 GB SanDisk Ultra with an 80 MB/s write speed. The integration of the SD card into the development kit was accomplished through the HW-125 microSD card module (Figure 3.2(d)) and file naming was provided by the date/time stamps taken from the DS3231 real-time clock (RTC) module (Figure 3.2(c)).

The development kit's Bluetooth connection utilized the HC-05 module, chosen for its maximum baud rate of 1,328,400. The HC-05 module is capable of functioning as both a slave and a master in the communication network (Figure 3.2(g)). In the system, data production amounted to 24 kB per second, and the Bluetooth module could achieve a data transmission rate of 132 kB per second. To optimize power consumption, specific parameters for the Bluetooth connection were configured. When searching for a device, the query time interval, query time, paging time interval, and paging time were set at 640 ms, 0.625 ms, 640 ms, and 0.625

ms, respectively. These values were chosen to ensure that the Bluetooth module consumes less power compared to its default parameter values. Once connected to a device, the Bluetooth was set to sniff mode, minimizing power consumption during idle periods while awaiting commands during communication. The parameters for the sniff mode included a maximum time of 125 ms, a minimum time of 6.25 ms, a test time of 1.25 ms, and a waiting time of 5 seconds.

3.2 Firmware Development for the Development Kit

In addition to Arduino libraries, open source libraries used in embedded software are as follows:

- SdFat, Author: Bill Greiman, Version: 2.1.2
- SparkFun MAX3010x Pulse and Proximity Sensor Library, Author: SparkFun Electronics, Version: 1.1.1
- DS3231, Author: Petre Rodan

Initially, the we focused on determining the time required to read data from the sensors, save it on the SD card, and transmit it via Bluetooth to achieve the desired sampling rates. I2C communication was established at a clock frequency of 400 kHz, dictated by the speed constraints of MAX30102. At this communication speed, samples could be read from both the infrared and red LEDs of the MAX30102 in approximately 0.9 ms, and from the X, Y, and Z axes of the ADXL355 in 0.6 ms. For analog data, it took around 0.15 ms to read one sample. The overall system included two MAX30102s, two ADXL355s, one ECG, and one temperature sensor. The ADXL355 and MAX30102 collected data at sample rates of 500 Hz and 200 Hz, respectively. The data collected by MAX30102 underwent on-chip sample averaging, resulting in an effective sampling rate of 50 Hz. The ECG was sampled at 500 Hz, and the temperature sensor was sampled at 1 Hz. It should be noted that in the first iteration of the firmware, all data points were stored as if they are all sampled at the highest sampling rate (500 Hz) due to the data structure being used. This was later changed in the finalized version of the firmware to a much more efficient data structure in terms of storage and processing power.

Given the timing specifications, the data acquisition from accelerometers (0.6 ms each) and the ECG sensor (0.15 ms) collectively accounted for 1.35 ms within a 2 ms cycle. When additional operations, such as writing data to the microSD card, sending data over Bluetooth, and reading data from MAX30102, were introduced, it became evident that timely data acquisition from sensors requiring a 500 Hz sampling rate was challenging. This resulted in data skipping when the FIFOs overflowed. To address this issue, an algorithm was devised. This algorithm calculated the time spent by the ATMEGA2560 in its statements. The primary timer-controlled statement, executing most frequently, needed to be completed in less than 2 ms to meet the 500 Hz sampling rate requirement. Any excess time spent beyond 2 ms was stored in a variable, incremented with each occurrence. If the calculated extra time surpassed 2 ms, the microcontroller was compelled to read from the FIFOs of the sensors and the virtual FIFO created for the ECG. This algorithm ensured that the microcontroller collected all available data from the sensors without missing any samples. This algorithm is no longer needed in the final version of the firmware as data structure became much more efficient.

The decision to employ a virtual FIFO for the ECG was prompted by the observation that ECG samples were not consistently collected at constant intervals due to variable statement execution times. This variability led to both data skipping and data shifting issues. By utilizing the FIFOs of the MAX30102 and ADXL355, data could be collected at the desired frequencies without any data shift. The previously described algorithm addressed the data skipping problem. However, the analog ECG sensor, lacking any storage element, encountered data skipping and small data shifts. To mitigate these issues, a virtual FIFO and timer interrupts were introduced. When data needed to be read from the ECG sensor, the ATMEGA2560 was interrupted by the timer, enabling the sampling of a data point from the ECG sensor at constant intervals. This sampled data point was then stored in the virtual buffer created for the ECG until it could be written to the microSD card and transmitted via Bluetooth. This approach ensured that ECG sampling occurred consistently.

Four distinct modes (*Start Recording*, *Pause Recording*, *Stop Recording* and *Low Power*) have been incorporated into the system through the utilization of buttons, with hardware interrupts serving to control recording capability and manage power consumption. In *Start Recording* mode, the system initiates data reading by generating a new file on the microSD card and proceeds to write the acquired data to this file. The name of the file is determined by the timestamp captured by the DS3231 RTC module. *Pause Recording* mode temporarily halts the ongoing recording process without closing the file. To resume recording, *Pause Recording* button should be pressed again. In *Stop Recording* mode, the created file is closed, and the recording process is halted. Simultaneously, the data written to the microSD card is sent both to Bluetooth via the serial port and to a PC via Bluetooth. For testing the Bluetooth connection with a PC, PuTTY was employed. The data displayed on PuTTY's console is logged and saved in a file. In the final mode, *Low Power* the system deactivates the sensors and communication channel buses, placing the microcontroller in a low-power mode to minimize power consumption.

3.3 Data Collection Protocol for the Development Kit

To test the development kit with human trials, an ethical approval was obtained from Koç University Ethics Comity with decision number 2021.284.IRB2.054. In the context of ethical approval, an 'Informed Consent Form' was prepared for participants to sign before the experiments. While the majority of human trials will be conducted with the PCB system, the system designed with the development kit was tested with two participants (one male and one female) with no history of cardiovascular or cardio respiratory diseases for five minutes each under basal (motionless) conditions.

The main body of the system (Figure 3.2(b)), consisting of a tri-axial accelerometer, PPG module, and temperature sensor, was affixed to the mid-sternum of the subject using hypoallergenic transparent medical tape. Additionally, three ECG cables were secured to the chest via gel electrodes, following the configuration outlined by Einthoven's triangle. Additionally, the daughter body (Figure 3.2(e)) comprising a tri-axial accelerometer and PPG module, was positioned on the wrist using the same medical tape. It is important to highlight that precise orientation of the accelerometers and proper skin contact for the PPG sensors were meticulously ensured before commencing data collection.

In addition to the signals acquired through the development kit, as illustrated in Figure 3.3, concurrent recordings of reference respiration and ECG signals were performed using the BIOPAC system (BIOPAC Systems, Inc., Goleta, CA, USA). The reference respiration signal was captured using a respiration effort transducer, while the reference ECG signal was obtained through three gel electrodes. Wireless transfer to the BIOPAC system was facilitated by the Bionomadix RSPEC-R module (BIOPAC Systems, Inc., Goleta, CA, USA). All reference signals were sampled at a rate of 500 Hz.

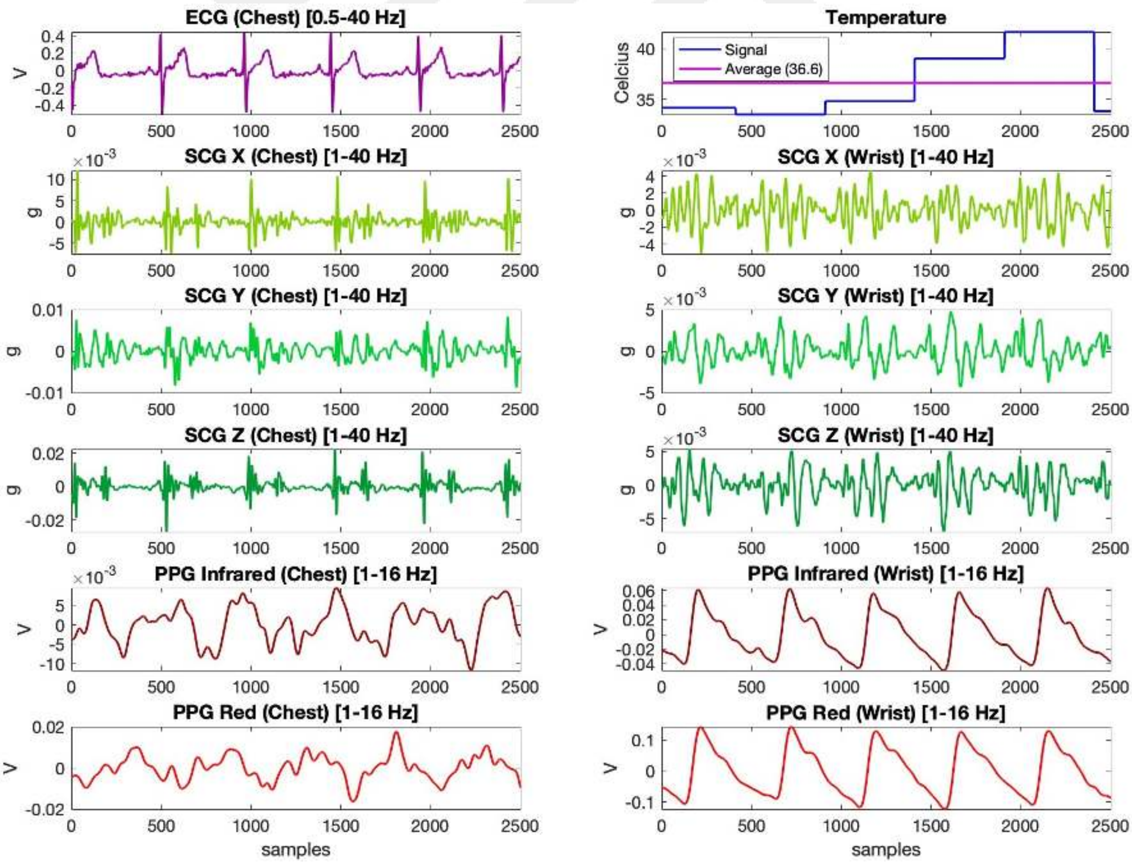

Figure 3.3: 5-second-long, pre-processed segments of the signals acquired with the development kit.

The recorded signals were processed using the formulas detailed in section 3.8 to calculate heart rate, heart rate variability, respiratory rate, oxygen saturation, and blood pressure.

3.4 Printed Circuit Board (PCB) Design

The PCB consists of 4 layers, following the arrangement of Signal-GND-GND-Signal. This configuration allows for a low-impedance ground (GND) plane, effectively reducing the impact of potential sources of electrical noise and providing proper return current paths. Lead-free hot air solder leveling (HASL) was preferred over the standard HASL to ensure that it does not contain lead, which could potentially be harmful to human health. Additionally, the PCB material is FR-4 TG155, which offers low inductance and a stable dielectric constant, making it a suitable choice for our application.

The PCB design of the main body attached to the chest is presented in Figure 3.4. Separate cards were designed for the PPG and temperature sensors to maximize their contact with the skin (Figure 3.5). Similarly, the PCB design of the additional body is presented in Figure 3.6.

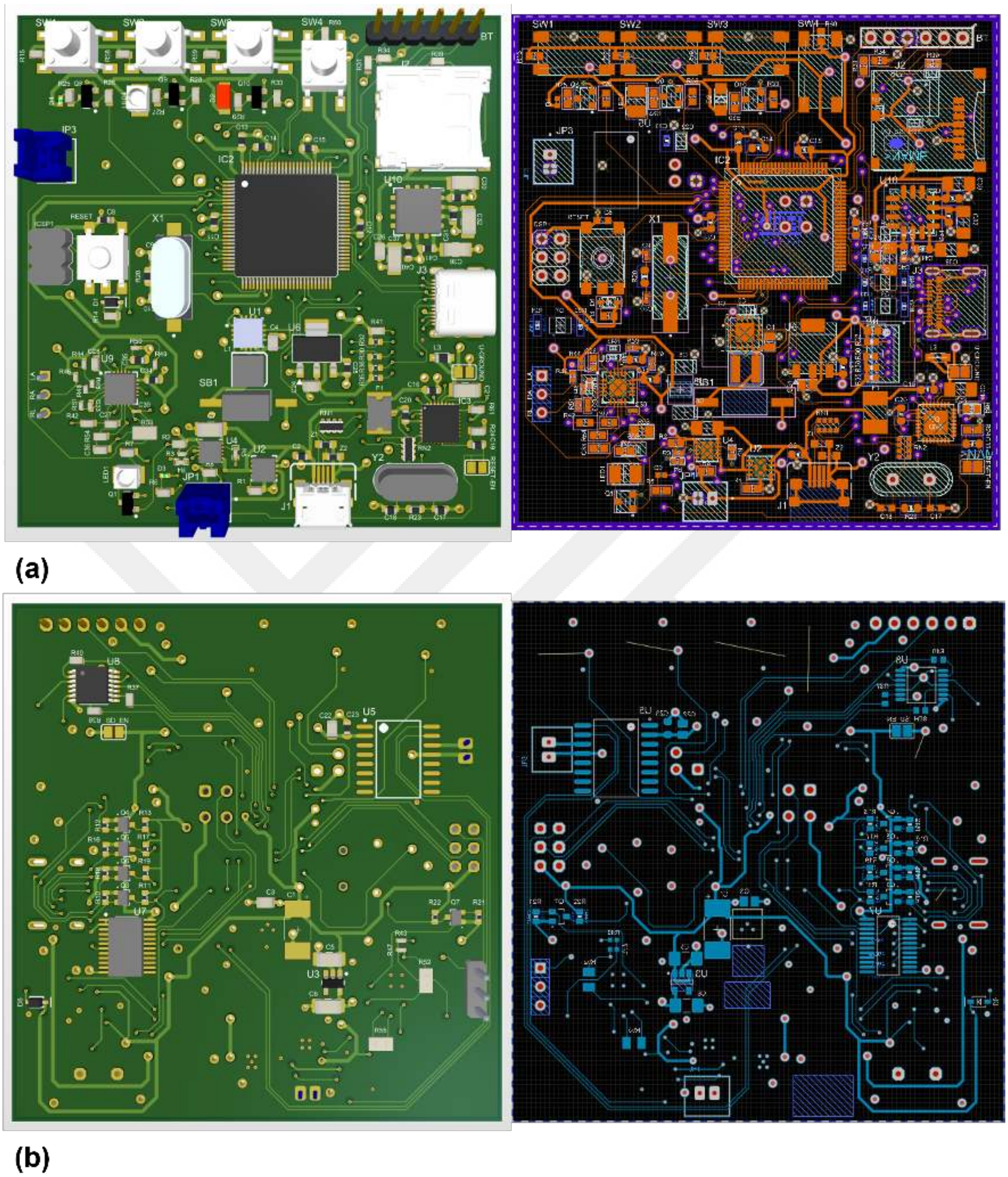

Figure 3.4: The PCB design of the main body fixed to the chest, (a) front and (b) back faces.

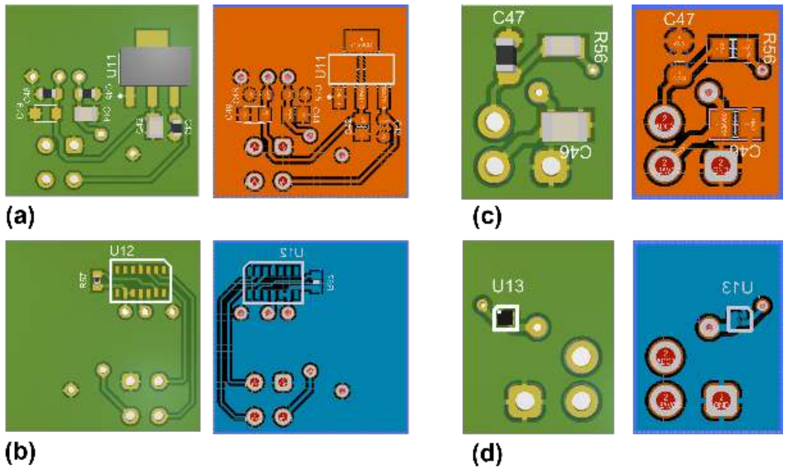

Figure 3.5: The front and back view of the PCBs containing the PPG system mounted on the main body, (a) front and (b) back faces, and the front and back view of the PCB containing the temperature sensor mounted on the main body, (c) front and (d) back faces.

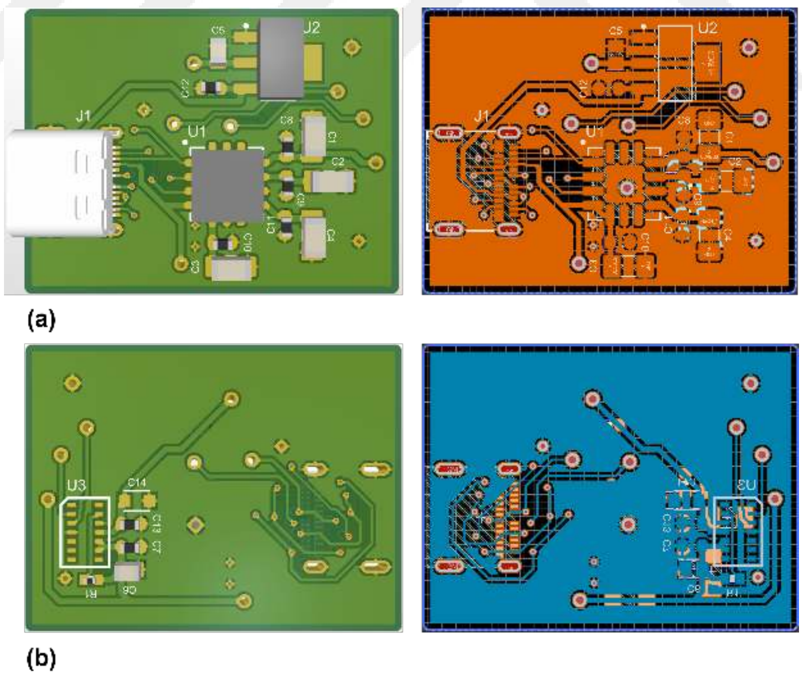

Figure 3.6: The PCB design of the daughter body and the front (a) and back (b) view of the PCB.

3.5 Changes to Firmware and Components After PCB Design

While transitioning from the development kit to the finalized PCB version, most of the embedded software codes were revised with major changes to how the data collection is handled by the microcontroller. Additionally, in the final version of the system, a different temperature sensor was used to enable more precise measurements. Similarly, a change was made on the choice of bluetooth device and RN-42 was preferred due to its customizable non-standard baud rates. The final hardware configuration of the system is presented in Figure 3.7.

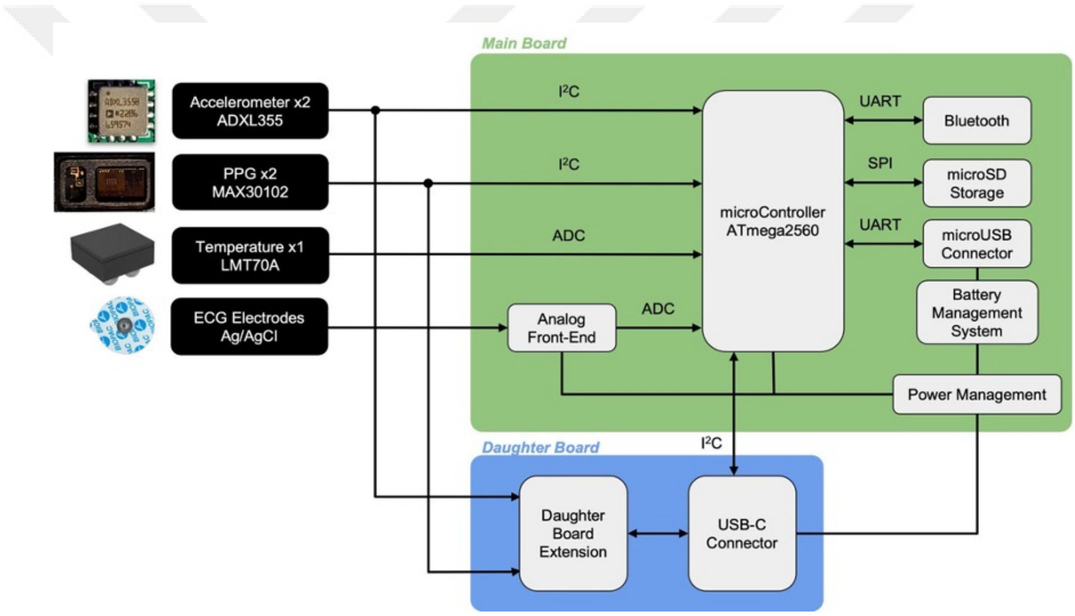

Figure 3.7: System overview and the details of sensor communication protocols.

3.5.1 Temperature Sensor

For body temperature measurement, analog LMT70A temperature sensor (Texas Instruments, Dallas, TX, USA) was selected, which offers an accuracy of ±0.05°C within the temperature range of 20°C to 42°C, a resolution of 5.194 mV/°C, an operating range from -55°C to 150°C, and a noise floor of 600 nV/$\sqrt{Hz}$. The signal was sampled by the microcontroller's ADC at 25 Hz and 10-bit resolution.

3.5.2 Data Storage and Transfer

The data from sensors is temporarily stored on the microcontroller's dynamic memory in 596-byte chunks, which correspond to 40 ms of data. After a chunk of data is collected, the data is written to a file on a microSD card and simultaneously streamed via Bluetooth. The Bluetooth allows us to stream the data in real time for monitoring the subject's data during the data collection protocol, which we had done using Matlab. This also allows for utilizing a PC's powerful processor to employ data processing and analysis algorithms in real time if the need arises, such as dynamic assessment of a subject during activity.

To make sure that no data was being dropped, we checked time-stamped data points for any inconsistencies and missing sections and compared the data stored in the microSD card with the data streamed via Bluetooth to see if there was any difference between the two. The data recordings were stored on the microSD successfully without any dropped samples.

Our design allows for the integration of external Bluetooth or Wi-Fi modules as long as they are capable of using UART communication protocol. For this work, we used the RN-42 for Bluetooth connection due to its customizable baud rate and availability. We set the baud rate to 1 MHz, which is compatible with the 16 MHz clock and transfers a chunk of data in roughly 4.8 ms. For power saving, the Bluetooth was set to use sniff mode. In sniff mode, the device goes into deep sleep and wakes up every 40 ms to send data. When it is not sending data, its current consumption is roughly at 2 mA, and when it is sending data, its current consumption is at 30 mA. We also set inquiry and page intervals to their lowest possible at 11.25 ms, reducing current consumption during device discovery from 20 mA to 5 mA.

3.5.3 Battery and Power Management

The system is powered by a single 400 mAh Lithium-Polymer (Li-Po) battery that has built-in circuitry for overcharge and overdischarge protection. The battery is charged through the microUSB connection, and the charging is managed by the LTC4062 (Analog Devices, Norwood, MA, USA) battery charger. Li-Po and Lithium-Ion batteries' nominal voltage is around 3.7 V, therefore, to power the 5 V circuitry in the system, the battery voltage is boosted to 5 V with the help of the TPS61092 (Texas Instruments, Dallas, TX, USA) boost converter.

3.5.4 Firmware Design

The accelerometer, ECG, PPG, and temperature sensors are sampled at rates of 500 Hz, 500 Hz, 200 Hz, and 25 Hz, respectively. The accelerometer and PPG sensors store data in FIFOs, and FIFOs are read by the microcontroller in chunks, as requesting subsequent bytes from sensors is faster due to overheads present in the I2C protocol. Since the data is stored in FIFOs, it is sampled at equal intervals at their respective sampling rates.

ECG and temperature sensors are analog. We used timer interrupts to sample analog data with the designated sampling rates. The use of interrupts is essential since they prevent any delays in sampling by temporarily halting all the processes and prioritizing the sampling operation. This is especially important for signals with high sampling frequencies, in our case, the ECG, since even small delays in the order of microseconds can adversely affect the sampled data due to uneven sample distances.

The data from sensors is stored in chunks in the microcontroller before being written to the microSD card. Most microSD cards use 512 or 1024-byte sectors. It is more efficient to write data to a microSD card in binary format and in 512-byte chunks. Therefore, we send our data to the microSD card in 512-byte chunks for faster write times. The same data chunk is also sent to the Bluetooth via universal asynchronous receiver/transmitter (UART) and displayed on a Matlab plot in real-time.

3.6 Final Version of the System and Case Design

3.6.1 3D Case Design

Blender (version 3.6) was used for the three-dimensional case design. Suitable gaps were created for buttons, micro USB, and microSD card inputs, as well as for PPG and temperature sensors. A three-section design was preferred for the main body to accommodate batteries and the Bluetooth module. A 3D render of the entire system is presented in Figure 3.8.

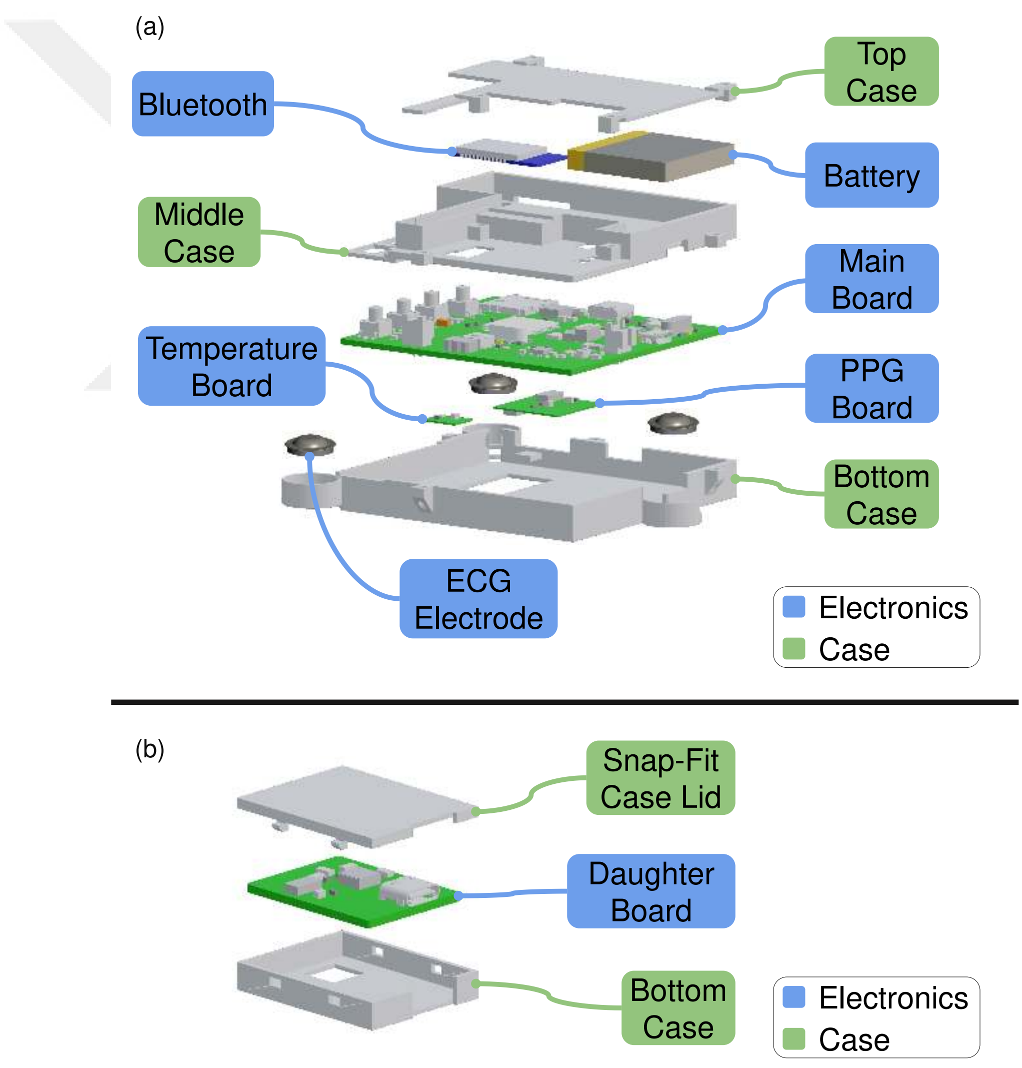

Figure 3.8: Renders of the (a) main and (b) daughter boards.

3.6.2 Finalization of the System

The Blender designs were 3D printed, and the entire system was assembled. The final form of the main body and the positions of the sensors are detailed in Figure 3.9. Three different views of the main body from different layers is shown in Figure 3.10, the positions of the sensors in the daughter body are illustrated in Figure 3.11, and the final state of the device is detailed in Figure 3.12.

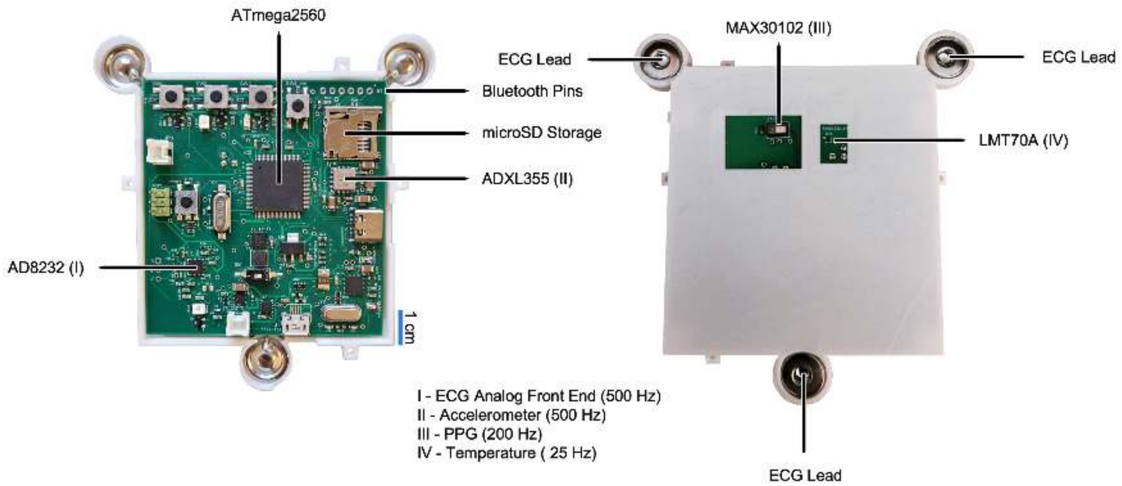

Figure 3.9: The design of the main body and locations of the corresponding sensors. The 3D-printed case is mounted on the mid-sternum using three gel electrodes, which are also used to acquire the ECG recordings.

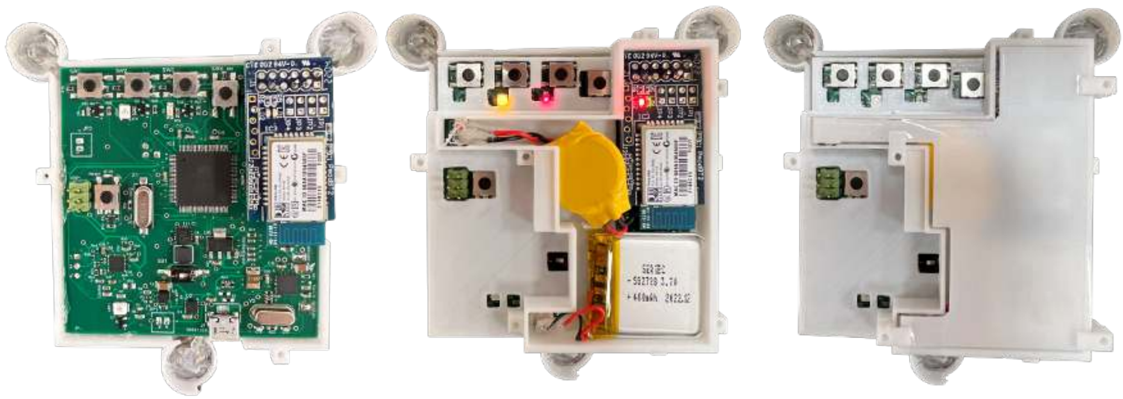

Figure 3.10: Finalized version of the device with three sections of the case design.

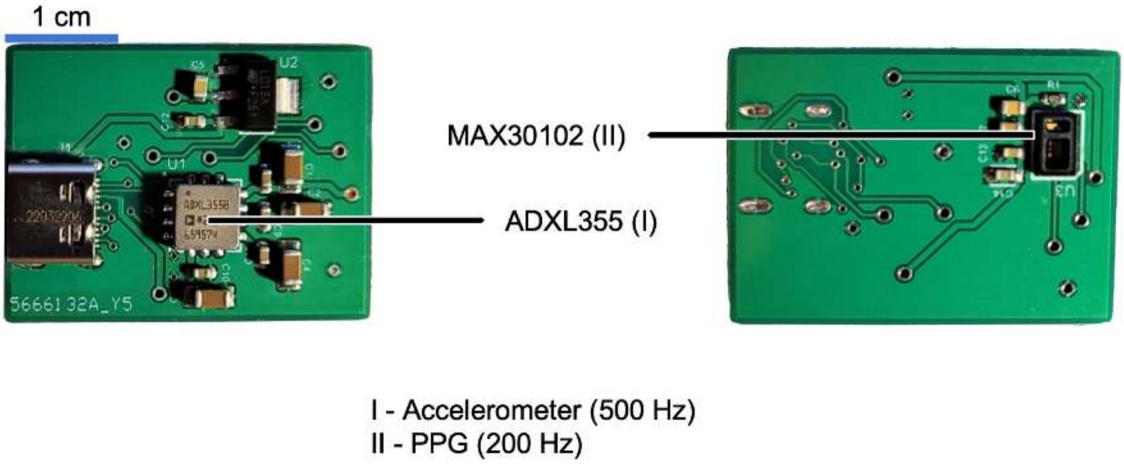

Figure 3.11: Daughter body sensor locations.

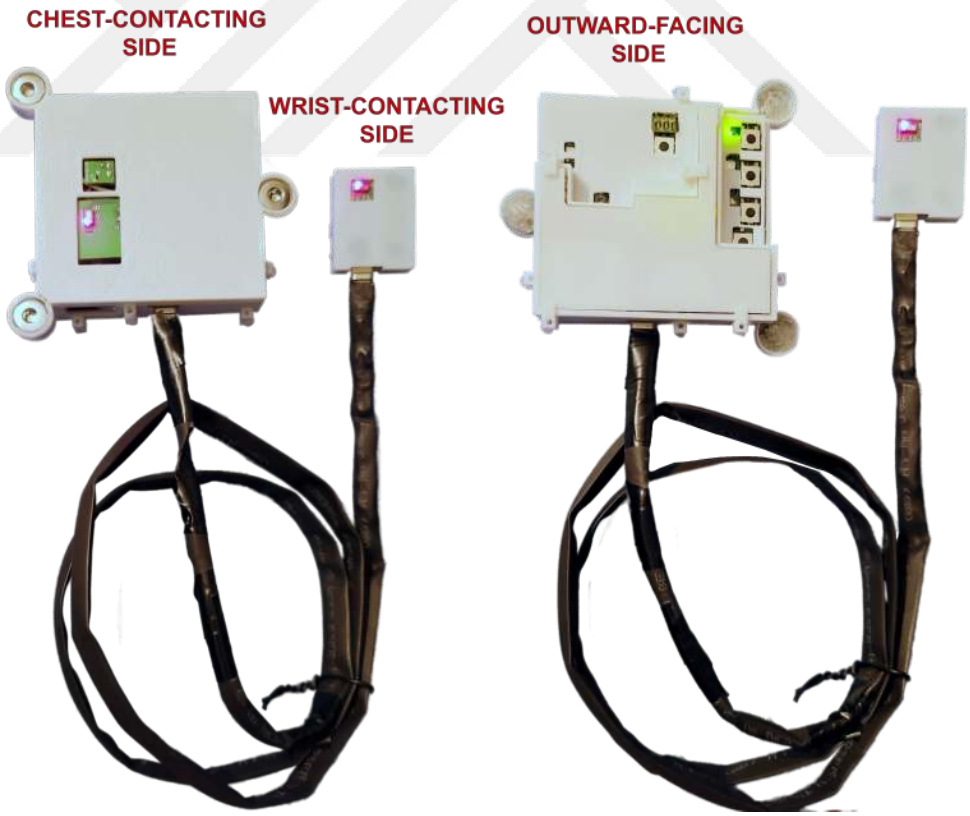

Figure 3.12: Finalized version of the device with the daughter body attached.

3.7 System Performance Experiments

Data collection was conducted following an approved protocol by the Koc University Institutional Review Board, and all participants provided their written consent. *PhysioPatch* was affixed to the chest region using three gel electrodes, while the daughter board was secured to the wrist area using Roll Trans Transparent Medical Tape. Reference ECG and respiration signals were acquired using the BIOPAC system. The RSPEC-R module of the BIOPAC system wirelessly transfers the chest and abdominal expansions/contractions measured through electrodes and a respiratory belt to the BIOPAC system.

Prior to commencing the experimental protocol, participants' age, weight, sex, and height were recorded. Subsequently, measurements for body temperature, oxygen saturation, heart rate, and systolic and diastolic blood pressure values (SBP and DBP) were taken. Comfort Non-contact Infrared Thermometer was used for temperature measurement, Comfort Plus Fingertip Pulse Oximeter for oxygen saturation, and the Omron M2 system for heart rate and blood pressure measurements. Oxygen saturation, heart rate, and blood pressure values were measured again after the completion of the experimental protocol.

Table 3.1: Subject demographics (8 females, 12 males)

	Age (years)	**Height (cm)**	**Weight (kg)**	**Temperature (°C)**
mean ± std	23.8 ± 4.2	172.6 ± 9.5	70.9 ± 16.1	36.6 ± 0.2
	SBP Before (mmHg)	**DBP Before (mmHg)**	**HR Before (bpm)**	**SpO2 Before (%)**
mean ± std	121.0 ± 13.3	79.5 ± 10.0	83.8 ± 14.3	98.6 ± 0.8
	SBP After (mmHg)	**DBP After (mmHg)**	**HR After (bpm)**	**SpO2 After (%)**
mean ± std	114.0 ± 12.1	76.1 ± 10.6	85.7 ± 14.2	98.4 ± 0.7

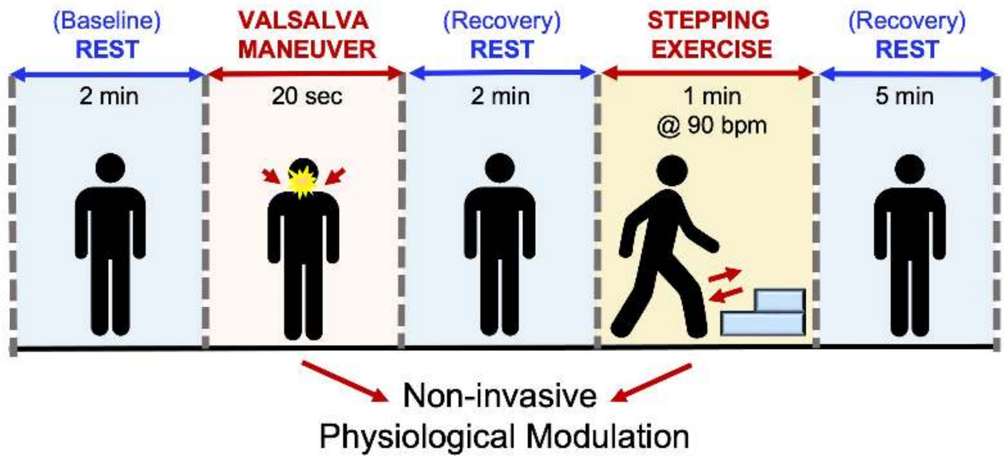

Figure 3.13: Experimental protocol.

The protocol employed for testing the system was designed to include multiple steps, aiming to measure both baseline signals when participants were stationary and the changes in the signals in response to physical modulations. After these modulations, physiological parameters return to their baseline values typically after a few minutes. In this study, the designed protocol includes the Valsalva maneuver and stepping exercise as the physiological modulation methods. The protocol is presented in Figure 3.13. First, the participants were asked to stand still for 2 minutes, followed by a 20-second breath hold. After a 2-minute recovery period, the step exercise was initiated, in which participants stepped up and down to a rhythm of 90 bpm, guided by a metronome. The experimental protocol was concluded with a 5-minute recovery period. Throughout the entire protocol, physiological signals obtained from the chest and the wrist were continuously recorded on the microSD card, and the BIOPAC system recorded reference signals. A total of 20 individuals (8 females and 12 males) participated in the experiments, and their demographic information along with the hemodynamic data measured before and after the experimental protocol are presented in Table 3.1.

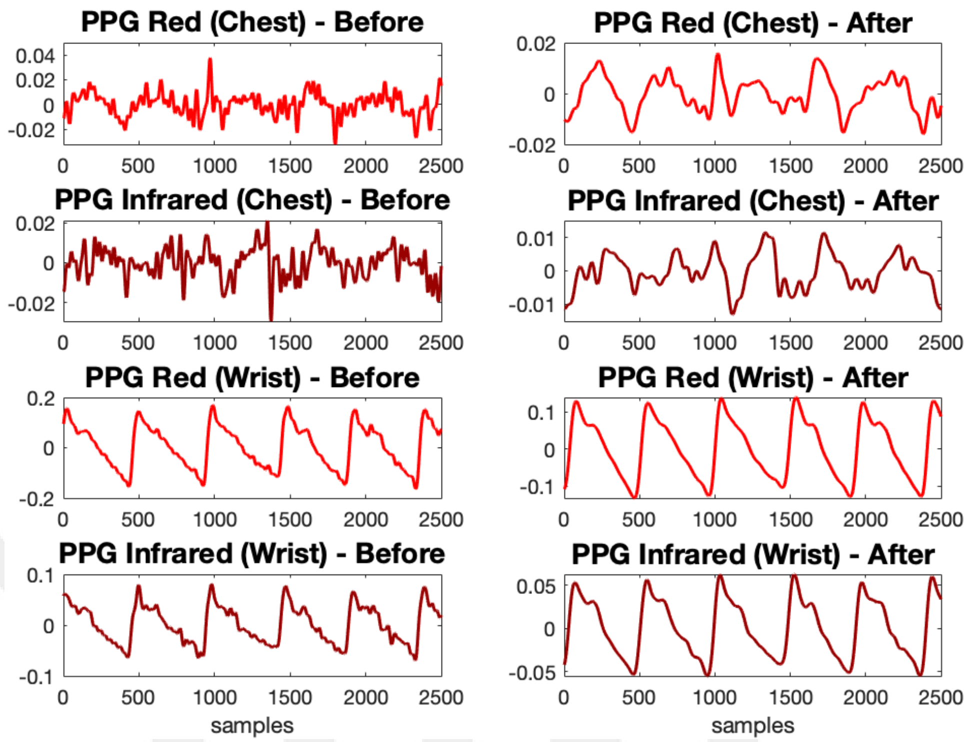

Figure 3.14: PPG signals before and after Gaussian filtering.

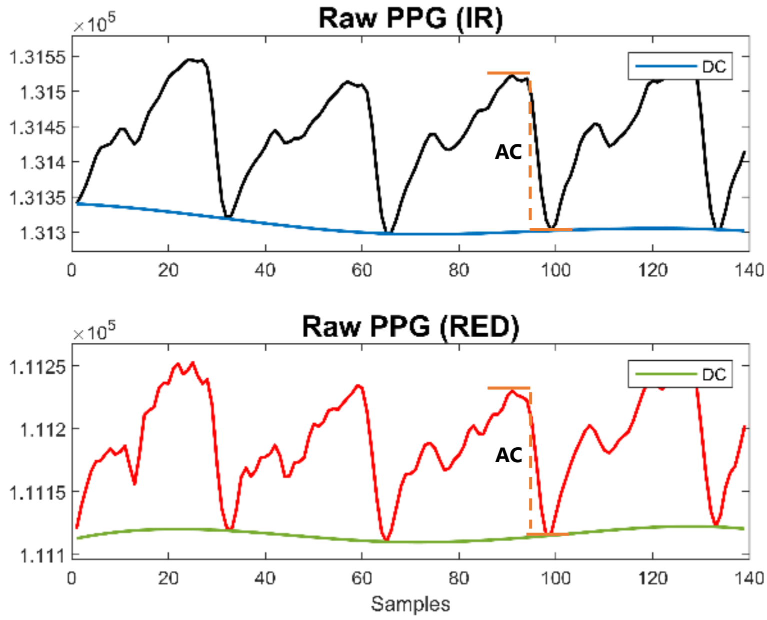

Figure 3.15: Determining the AC and DC components on the PPG signals for oxygen saturation calculation.

3.8 Data Analysis

Throughout the entire data collection process (including the modulations), the *PhysioPatch* was affixed to the chest and wrist. There was no discomfort observed, thus the ease of use was confirmed. On the other hand, as the primary aim was to validate the performance of *PhysioPatch*, only the baseline rest period was used to assess the quality of the signals and accuracy of the algorithms in derivation of hemodynamic parameters.

3.8.1 Preprocessing

Pre-processing algorithms were designed to enable the extraction of information regarding respiratory, cardiac, and circulatory system health from the signals recorded through the *PhysioPatch* device. The obtained parameters were then compared with the recorded reference values. The algorithms were tested on the signals recorded from 20 participants using the designed system. Following the experiments, the most suitable frequency ranges for signal filtering were determined in accordance with the values in the literature [Carek et al., 2017, Pandia et al., 2012, Shandhi et al., 2019]. Finite impulse response (FIR) Kaiser window band-pass filters were employed for signal filtration. Selected frequency ranges were as follows:

- SCG: 1 - 40 Hz for vibration and acoustical information
- SCG: 0 - 1 Hz for respiration
- ECG: 0.5 - 40 Hz
- PPG: 1 - 16 Hz for oxygen saturation derivation
- PPG: 0 - 1 Hz for respiration

Additionally, we observed that the PPG signals obtained from the chest exhibit a high level of noise, making the identification of peaks and dicrotic notches more challenging compared to the PPG signals obtained from the wrist. This was expected, as accessing the vascular region in the chest area is inherently more difficult compared to the wrist. To smooth the artifacts in the signals, a Gaussian window was employed. The improvements in the signals after the application of the Gaussian window are illustrated in Figure 3.14.

3.8.2 Heart Rate and Heart Rate Variability Derivation

To compute the heart rate and heart rate variability values from the collected signals, the following steps were implemented:

1. First, the reference HR and HRV values were computed using the reference ECG signal obtained with the BIOPAC system. To that end, the R-peaks on the ECG signal were detected, and the durations between the consecutive R-peaks were calculated to form an RR vector. Equations 3.1 and 3.2 were then applied to this vector to calculate the heart rate in beats per minute and heart rate variability in milliseconds.

$$HR = \frac{60 * F_s}{mean(RR)} \tag{3.1}$$

$$HRV = \frac{F_s}{std(RR)} * 1000 \tag{3.2}$$

$$\%\, error = \frac{actual - calculated}{actual} * 100 \tag{3.3}$$

2. Following the computation of the reference values, HR and HRV were determined from the ECG signal recorded with the *PhysioPatch* using the same formulas.

3. Finally, the HR and HRV values were extracted from the PPG signals obtained through the system, captured both from the wrist and the chest. The calculation involved determining the time intervals between the consecutive peaks

on the Gaussian-windowed red and infrared PPG signals, resulting in a PP vector analogous to the previously generated RR vector. The HR and HRV values were then computed using the same formulas, with the substitution of the PP vector instead of the RR vector.

4. Equation 3.3 was used to compute the percentage error (%error), with "actual" representing the reference HR and HRV values, and "calculated" representing the values computed using the ECG, PPG-red, and PPG-infrared signals obtained from the patch. *(Fs: sampling rate, std: standard deviation)*

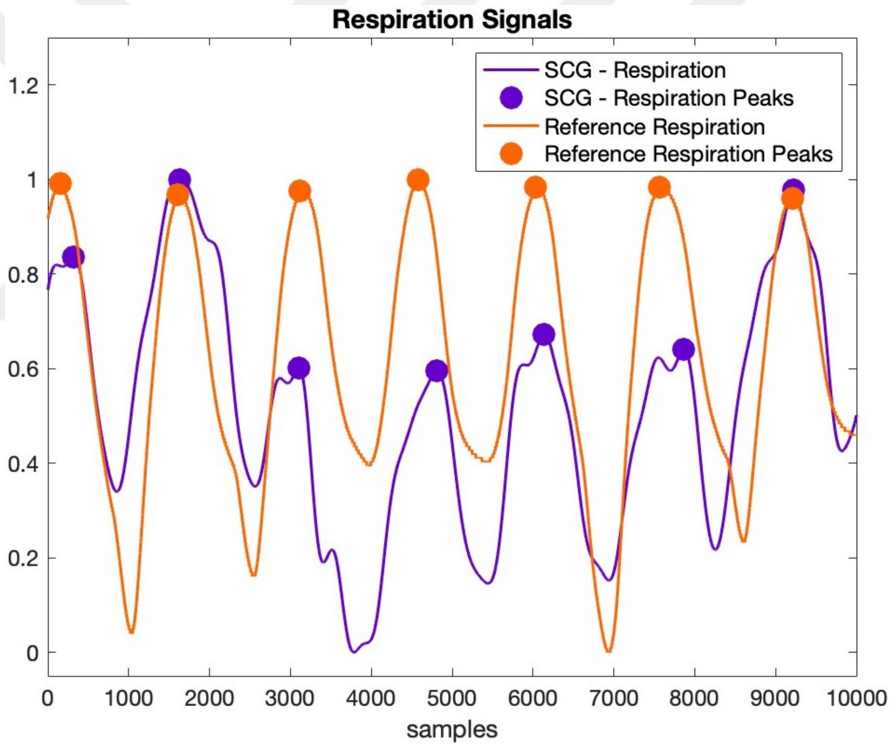

Figure 3.16: Comparison of the reference and SCG-derived respiratory signals.

3.8.3 Respiration Rate Derivation

Two different approaches were employed to calculate the respiration rate. In the first approach, the PPG-red signal taken from the chest was leveraged. The signal was filtered within the 0 - 1 Hz range and smoothed with Gaussian window. In the the second approach, the SCG signal, filtered within the 0 - 1 Hz range, was used to extract respiratory information. The analysis was conducted along the dorso-ventral axis, in accordance with established literature practices [Pandia et al., 2012]. Similar to the approach used in the PPG case, Gaussian windowing was applied to the SCG signal to smooth the signal. Utilizing the peaks identified in these signals, the reference, PPG-derived, and SCG-derived respiration rates (the number of exhalation-inhalation cycles per minute) were calculated. 20-second-long segments from the reference and SCG-derived respiration signals from one of the subjects were presented in Figure 3.16.

3.8.4 Oxygen Saturation Computation

Using the PPG waves recorded using the red and infrared LEDs, one can obtain information about the oxygen retention state of hemoglobin [de Armendi and Govindaraj, 2017]. Oxygenated (HbO_2) and deoxygenated (Hb) hemoglobin have different properties that allow different absorption levels of red and infrared light. Using the DC values and AC amplitudes of these two different waves, it is possible to calculate the normalized absorption ratio (R) as shown in Equation 3.4.

$$R = \frac{\frac{AC_{red}}{DC_{red}}}{\frac{AC_{IR}}{DC_{IR}}} \tag{3.4}$$

Figure 3.15 shows the DC and AC components on the red and infrared signal slices. Equation 3.5, provided by Analog Devices for the MAX30102, was used to calculate the oxygen saturation (SpO_2) levels.

$$SpO2 = -45.060 * R^2 + 30.354 * R + 94.845 \tag{3.5}$$

The challenge here is to detect the PPG peaks, as the PPG signal is easily corruptible by motion artifacts and ambient light. PPG must be carefully placed where capillaries and arteries are. Special care must be taken so that PPG firmly contacts the measurement area and also does not apply too much pressure to the area to not disturb blood flow.

As previously detailed, the PPG signal was filtered using a finite impulse response (FIR) band-pass filter with cut-off frequencies at 1 Hz and 16 Hz. PPG peaks were detected in the filtered section. Then, the peak-to-peak value was calculated as the AC component. The DC part of the PPG was acquired by employing an envelope detector on the raw signal, as we found it to be better at extracting the DC component compared to a low-pass filter. The peak locations were used to find where the peaks correspond to in the DC component. The SpO_2 value was then calculated for each peak according to Equation 3.5.

3.8.5 Blood Pressure Estimation

In the development of methods for blood pressure estimation, initially an online dataset was used. The dataset we used, published by Liang et al., consists of 657 recordings from 219 subjects [Liang et al., 2022]. Each subject first had their arterial blood pressure measured using the Omron HEM-7201 (Omron Company, Kyoto, Japan) followed by three, 2.1-second-long PPG recordings in the span of three minutes. The PPG recording quality was evaluated by the authors of the dataset using a skewness signal quality index.

Preprocessing

The raw PPG values from the dataset had high frequency noise contaminating the signal. Low frequency baseline wander was also present in the recordings. Therefore, we conducted a filtering operation before using the dataset to train our BP estimation algorithm. A 4th order Butterworth filter was used with cut-offs at 0.4 Hz and 20 Hz. The resulting clean signal is shown in Figure 3.17. In the literature, it has been shown that the PPG signal can be adequately analyzed within these frequency ranges [Reali et al., 2022].

Also, deep learning algorithms greatly benefit from normalization. We normalized the data to limit the scale and reduce the variance according to the equation below, where μ is the mean and σ is the standard deviation (Equation 3.6).

$$x_{normalized} = \frac{x - \mu}{\sigma} \tag{3.6}$$

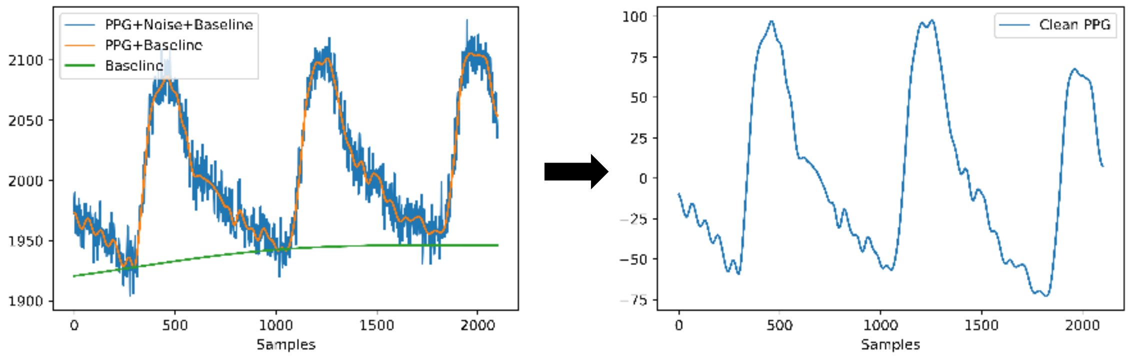

Figure 3.17: PPG Signal after preprocessing.

Machine Learning Algorithms

1. CNNs and their application over 1D data is not an unexplored topic. However, due to the popularity and success of 2D CNNs, conventionally, 1D data is transformed into 2D graphs (such as spectrograms) for analysis. Recently, the use of 1D CNNs for 1D data has become more common in the literature. This is in part due to 1D CNNs requiring less computational complexity and memory, making them a suitable candidate to use for lightweight, real-time applications without requiring specialized hardware. They are also easier to train than 2D CNNs, often requiring a smaller dataset. They have been used in time-series data analysis such as speech recognition, ECG monitoring, and stock value forecasting [Kiranyaz et al., 2021].

2. LSTMs are proposed as a solution to the exploding/vanishing gradient problem of Recurrent Neural Networks (RNNs). Its ability to remember longer dependencies is a result of its recurrently connected memory blocks that regulate the flow of information via non-linear gating units. For this reason, it's a popular choice for handling time series data [Van Houdt et al., 2020].

3. CNN-LSTM hybrid models take advantage of both architectures. CNNs provide LSTMs with extracted features with a reduced dimensionality that adequately represents the input, while LSTMs capture temporal dependencies over long sequences. The hybrid architecture consistently outperformed conventional unmixed CNN and LSTM architectures [Van Houdt et al., 2020]. In the literature, the hybrid model has been used for classification of plant growth status [Xing et al., 2023], forecasting of photovoltaic power production, emotion identification, etc. [Van Houdt et al., 2020, Agga et al., 2022]. Bao et al. have successfully demonstrated that a hybrid model can successfully estimate wrist angles from electromyogram (EMG) signals [Bao et al., 2020]. They compared their hybrid model with support vector regression (SVR), Random Forest, CNNs, and LSTMs. Their hybrid model outperformed all other models in all trials and protocols.

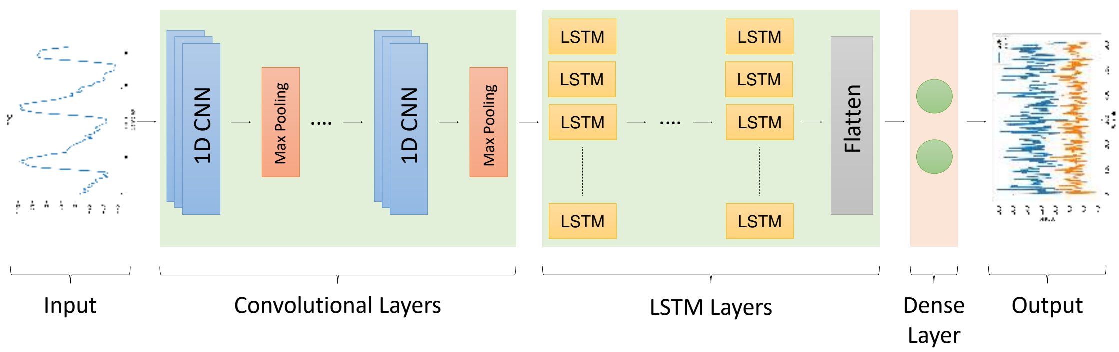

Figure 3.18: General Structure of the Model.

We propose a CNN-LSTM hybrid network to solve the BP estimation problem. LSTMs and CNNs are highly popular deep learning techniques and have a variety of use cases ranging from natural language processing to image processing. LSTMs' ability to capture dependencies in long temporal sequences makes them a good match for time series estimation applications. CNNs' can extract learned features from the raw data. In theory, a hybrid model consisting of both should be able to extract the local features of a signal and capture the long-term dependencies.

Table 3.2: List of selectable hyperparameters.

Hyperparameters	**Hyperparameter Values**
1D CNN Layers	1, 3
1D CNN Filters	16, 32, 64
1D CNN Kernel Sizes	5, 15, 63
Lstm Layers	1, 3, 5
Lstm Units	32, 64, 128
Dense Layers	0, 1, 3
Dense Units	16, 64, 128

Hyperparameter Selection

The general structure of the model is presented in Figure 3.18. To tune the hyperparameters for our model, we conducted a random search on the hyperparameters in Table 3.2, training 100 different models over 30 epochs on the dataset.

The resulting architecture with the smallest validation root mean square error was selected as the candidate to be further trained on the dataset. The random search yielded the parameters in Table 3.3 for the model.

We have two neurons as the last layer of our architecture to output SBP and DBP values.

Evaluation

For a more reliable estimation of our model's performance, we used 10-fold cross-validation. The metrics used to evaluate the algorithm's performance are presented below, where y is the ground truth, x is the prediction, and n is the number of samples.

1. Mean Absolute Error (MAE): The mean of absolute errors (Equation 3.7).

$$MAE = \frac{1}{n}\sum_{i=1}^{n}|y_i - x_i| \tag{3.7}$$

Table 3.3: Hyperparameter selection results.

Hyperparameters	**Hyperparameter Values**
1D CNN Layers	3
1D CNN Filters	Layer 1: 16 Layer 2: 32 Layer 3: 64
1D CNN Kernel Sizes	Layer 1: 63 Layer 2: 15 Layer 3: 15
Lstm Layers	5
Lstm Units	Layer 1: 128 Layer 2: 128 Layer 3: 32 Layer 4: 64 Layer 5: 128
Dense Layers	0
Dense Units	–

2. Root Mean Square Error (RMSE): The standard deviation of prediction errors. It measures how spread the residuals are (Equation 3.8).

$$RMSE = \sqrt{\frac{1}{n}\sum_{i=1}^{n}(y_i - x_i)^2} \tag{3.8}$$

3. Mean Absolute Percentage Error (MAPE): The percentage mean of absolute errors (Equation 3.9).

$$MAPE = \frac{1}{n}\sum_{i=1}^{n}|\frac{y_i - x_i}{y_i}| \tag{3.9}$$

We used MSE (square of RMSE) to monitor the prediction success of the algorithm during training.

Table 3.4: Comparison of model performance. *(w/o opt: without optimization, w opt: with optimization)*

Model	**Performance Criteria**	**Systolic BP**	**Diastolic BP**
RelieF GPR (w/o opt)	MAE (mmHg)	10.08	7.87
	RMSE (mmHg)	14.80	9.83
	ME+STD (mmHg)	-	-
	MAPE (%)	-	-
CFS GPR (w/o opt)	MAE	11.91	7.64
	RMSE	16.05	9.16
	ME+STD	-	-
	MAPE	-	-
RelieF GPR (w opt)	MAE	3.02	1.74
	RMSE	6.74	3.59
	ME+STD	-	-
	MAPE	-	-
LightBGM	MAE	13.06	8.16
	RMSE	-	-
	ME+STD	0.00±16.95	-0.04±10.30
	MAPE	-	-
AdaBoost	MAE	13.22	8.04
	RMSE	-	-
	ME+STD	-0.56±16.95	-0.16±10.25
	MAPE	-	-
ResNet	MAE	13.62	8.61
	RMSE	-	-
	ME+STD	-1.85±17.45	-2.17±10.81
	MAPE	-	-
Ours	MAE	14.13	8.80
	RMSE	18.13	10.96
	ME+STD	0.71±18.23	-0.79±11.08
	MAPE	11.24%	12.54%

BP Estimation Results on the Dataset

In this section, a comparative analysis of our algorithm's performance is presented. We selected two papers using the same dataset as ours; therefore, the evaluation criteria that would normally be dependent on data distribution to draw conclusions, such as MAE, makes sense. Although most BP datasets have a similar range, depending on the subject demographics, the difference in the distribution of BP can be significant enough to skew conclusions drawn from different datasets. Our motivation was to prevent such an occasion from occurring.

Table 3.4 lists some of the best algorithms belonging to the two papers that used the same dataset as ours. Among them, only ours and [González et al., 2023]'s ResNet approach don't use any feature extraction prior to training. Our approach and [González et al., 2023]'s ResNet approach show very similar performances, with ours having better mean errors but slightly worse standard deviations. The rest of the machine learning approaches that utilize some kind of feature extraction method prior to training have better results in general. This might be due to deep learning-based approaches requiring a larger dataset to better understand the relationship between the input and output.

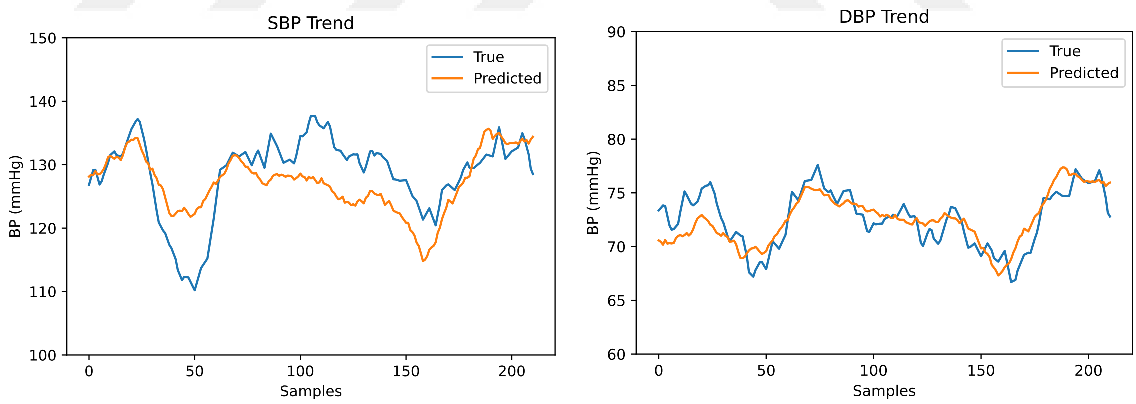

(a) (b)

Figure 3.19: (a) SBP Trends, (b) DBP Trends.

Figures 3.19 (a)-(b) show trends in four folds of the test data. The figures show that our algorithm can properly encapsulate the upward and downward movements in the blood pressure. The data was smoothed with a moving average filter (n = 30) to make the trend clearer in the visualization.

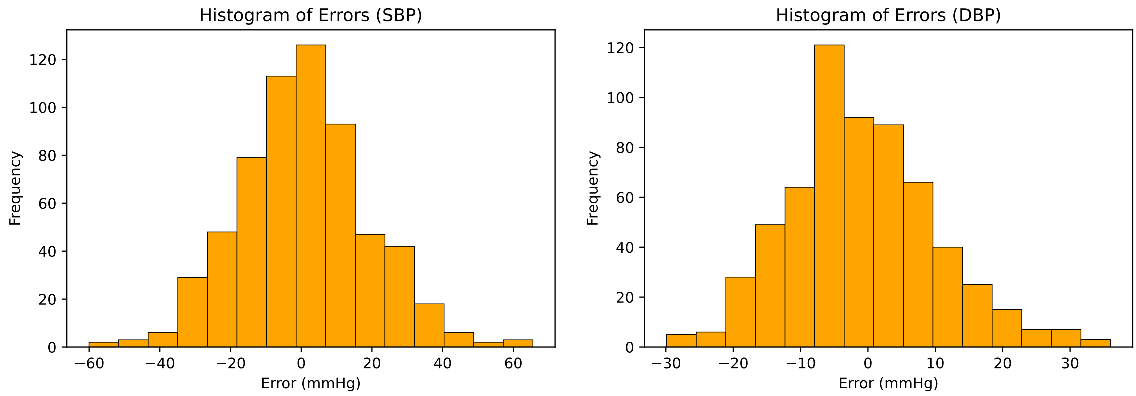

(a) (b)

Figure 3.20: (a) SBP Error Histogram, (b) DBP Error Histogram.

Figures 3.20 (a)-(b) visualize the histograms of residual errors. The error histograms indicate that the errors are normally distributed around 0. The error histogram of SBP has a higher range. This is because SBP has a higher variance as a result of its larger magnitude in comparison to DBP.

Chapter 4

RESULTS

4.1 Signal Quality and Data Transfer

The preprocessed 5-second segments of signals recorded through the device are presented in Figure 4.2. As seen from the graphs, physiological signals were successfully acquired at the desired sampling rates. Additionally, sample SCG signals recorded on the SD card and transferred to the computer via Bluetooth are presented in Figure 4.1. The data transmitted via Bluetooth resulted in a 100% correlation with the recordings on the microSD, with no dropped or skipped samples, showcasing the reliability of wireless data transfer. Despite the large number of sensors, the absence of data loss is a promising outcome for future iterations of the system.

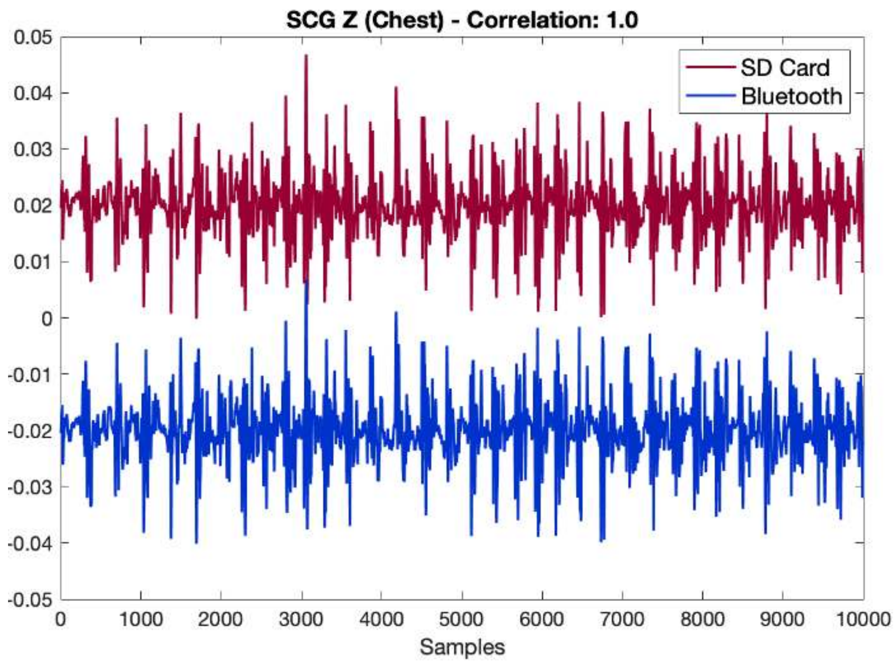

Figure 4.1: Comparison of the signals written to the microSD card and transferred to the computer via Bluetooth.

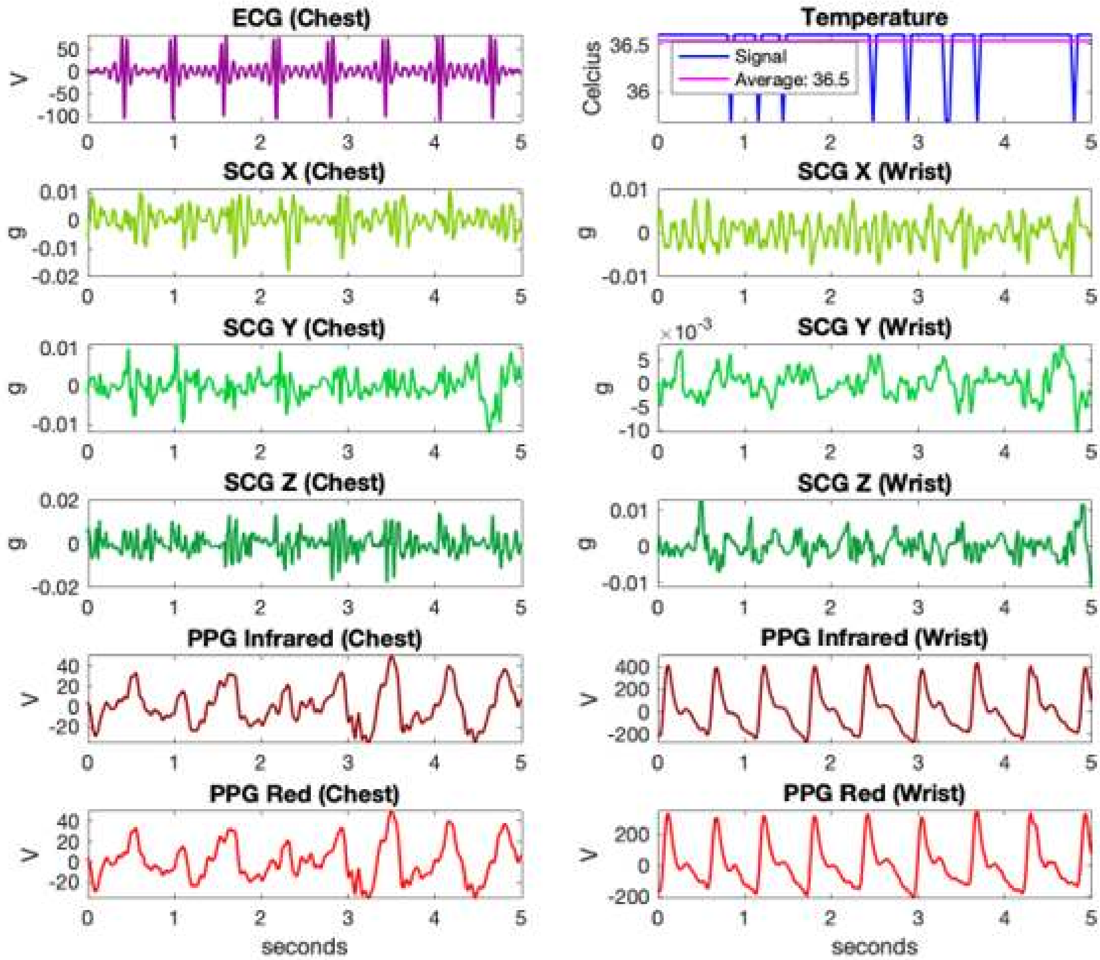

Figure 4.2: Preprocessed 5-second long signal segments.

4.2 *Comparison with Reference Measurements*

Table 4.1: Estimation Errors in % (mean ± std)

Heart Rate				
ECG	**PPG IR (Chest)**	**PPG Red (Chest)**	**PPG IR (Wrist)**	**PPG Red (Wrist)**
0.25±0.35	11.69±10.90	14.11±10.85	6.38±9.74	8.47±12.65
	Respiration		**SpO2**	
	SCGz (Chest)	**PPG (Chest)**	**Before**	**After**
	4.31±3.54	3.56±3.44	2.03±3.43	2.22±3.50
	Heart Rate Variability (ECG)		**Temperature**	
	5.03±6.32		3.21±2.45	

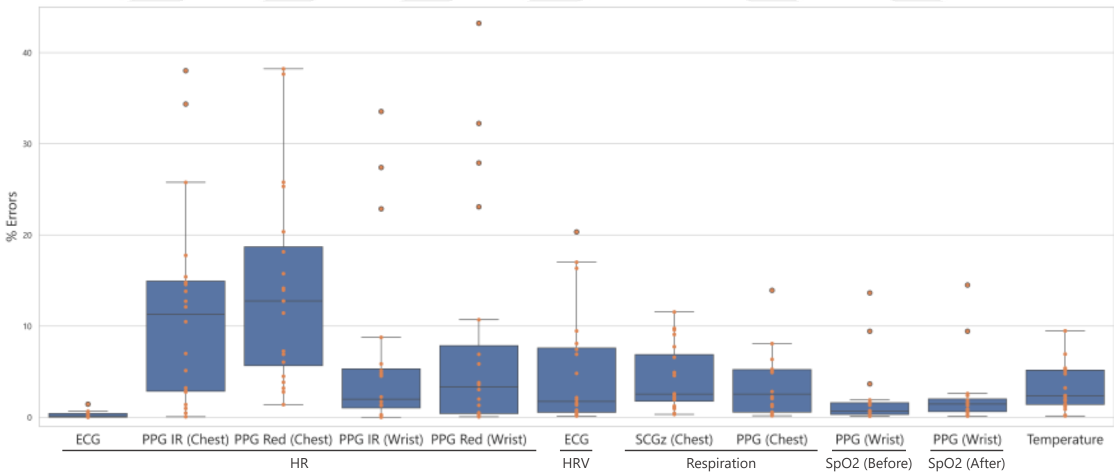

Figure 4.3: Boxplots showing the estimation errors and their distribution among different subjects. For any parameter, each circle corresponds to a different subject.

4.2.1 Heart Rate and Heart Rate Variability

Initially, the patch's performance in estimating HR and HRV values based on the acquired ECG and PPG signals was evaluated. As outlined in Section 3.8.2, HR and HRV were derived by calculating the time intervals between consecutive peak locations on the PPG and ECG signals. The reference HR and HRV values were determined using the peak locations on the ECG obtained with the BIOPAC system. The resulting % errors in HR estimation are presented in Table 4.1 and Figure 4.3. The low margin of error between the reference and *PhysioPatch*-derived values demonstrates the system's high performance. In particular, there exists an average error of 0.25%±0.35% between the reference HR values and those derived from ECG signals acquired from the chest, whereas for the PPGs, we observe a worse performance. Indeed, the chest PPG performed the worst as it was more prone to artifacts. Nonetheless, the HR values obtained from the chest ECG and wrist PPG exhibited negligible errors in the majority of cases, aligning closely with the reference HR measurements. Similarly, the HRV derived from the system's ECG resulted in a low % error of 5.03±6.32 as presented in Table 4.1.

4.2.2 Respiration Rate

Table 4.1 provides the average number of breaths per minute for the subjects based on the reference, SCG and chest PPG signals. The nearly identical number of respiration cycles shows that the system is able to capture respiratory information effectively.

4.2.3 SpO_2 Measurements

The calculation of the oxygen saturation utilized red and infrared PPG data obtained from the wrist. These values were compared with the reference values measured at the beginning and end of the protocol. The results obtained are presented in Table 4.1. Upon examining the average percentage errors, errors at levels of 2.03% (before) and 2.22% (after) were obtained.

4.2.4 Temperature Measurements

Reference temperature values from 20 participants were measured before the start of the experimental protocol. Accordingly, the average of temperature values obtained from the initial rest part of the device was calculated. The average error level was calculated to be 3.21% (Table 4.1).

4.2.5 Blood Pressure Measurements

For the calculation of systolic and diastolic blood pressure values for 20 participants, the CNN-LSTM approach detailed in section 3.8.5 was employed. The trained and tested model was also evaluated on the infrared wrist PPG data obtained from 20 individuals through the *PhysioPatch*. These values were compared with SBP and DBP measurements taken before and after the experimental protocol. SBP yielded errors of 9.45% (before) and 17.51% (after), while DBP yielded errors of 12.02% (before) and 12.51% (after). Since the blood pressure values were calculated using PPG signals recorded during the initial rest period, lower percentage error values were expected for the values obtained before compared to those obtained after.

Chapter 5

DISCUSSION AND CONCLUSIONS

In this thesis, an adaptable wearable patch prototype has been developed to facilitate comprehensive cardiovascular and cardiopulmonary monitoring which allows simultaneous acquisition of ECG, PPG, SCG, and body temperature signals. The design incorporates a main body affixed to the mid-sternum for collecting proximal ECG, SCG, PPG, and body temperature signals, and a detachable daughter body for distal SCG and PPG measurements, enhancing the scope of health assessment. Respiration rate, HR, HRV, SpO_2, blood pressure, and temperature values were computed from the data of twenty subjects using the patch and were compared with the reference values acquired through the BIOPAC and other measurement systems. The consistent low margin of error in all cases shows the high performance of the prototype and the effectiveness of signal improvement methods. Furthermore, the data transmitted via Bluetooth was consistent with the recordings on the microSD, with no dropped or skipped samples, showcasing the reliability of wireless data transfer. Despite the large number of sensors, the absence of data loss is a promising outcome for future iterations of the system.

Future work will concentrate on improving the battery life and finding better methods for affixing the system to the subject for less artifacts, especially for the PPG measurements. Such a system holds the potential to be convenient for patients and healthcare professionals, facilitating continuous health monitoring irrespective of time and environmental stressors, allowing for the extraction of important biological markers.

BIBLIOGRAPHY

[Agga et al., 2022] Agga, A., Abbou, A., Labbadi, M., El Houm, Y., and Ali, I. H. O. (2022). Cnn-lstm: An efficient hybrid deep learning architecture for predicting short-term photovoltaic power production. *Electric Power Systems Research*, 208:107908.

[Bai et al., 2018] Bai, Y., Hibbing, P., Mantis, C., and Welk, G. J. (2018). Comparative evaluation of heart rate-based monitors: Apple watch vs fitbit charge hr. *Journal of sports sciences*, 36(15):1734–1741.

[Bao et al., 2020] Bao, T., Zaidi, S. A. R., Xie, S., Yang, P., and Zhang, Z.-Q. (2020). A cnn-lstm hybrid model for wrist kinematics estimation using surface electromyography. *IEEE Transactions on Instrumentation and Measurement*, 70:1–9.

[Barrett et al., 2014] Barrett, P. M., Komatireddy, R., Haaser, S., Topol, S., Sheard, J., Encinas, J., Fought, A. J., and Topol, E. J. (2014). Comparison of 24-hour holter monitoring with 14-day novel adhesive patch electrocardiographic monitoring. *The American journal of medicine*, 127(1):95–e11.

[Carek et al., 2017] Carek, A. M., Conant, J., Joshi, A., Kang, H., and Inan, O. T. (2017). Seismowatch: wearable cuffless blood pressure monitoring using pulse transit time. *Proceedings of the ACM on interactive, mobile, wearable and ubiquitous technologies*, 1(3):1–16.

[Castiglioni et al., 2007] Castiglioni, P., Faini, A., Parati, G., and Di Rienzo, M. (2007). Wearable seismocardiography. In *2007 29th annual international conference of the IEEE engineering in medicine and biology society*, pages 3954–3957. IEEE.

[cheol Jeong et al., 2018] cheol Jeong, I., Bychkov, D., and Searson, P. C. (2018). Wearable devices for precision medicine and health state monitoring. *IEEE Transactions on Biomedical Engineering*, 66(5):1242–1258.

[Da He et al., 2011] Da He, D., Winokur, E. S., and Sodini, C. G. (2011). A continuous, wearable, and wireless heart monitor using head ballistocardiogram (bcg) and head electrocardiogram (ecg). In *2011 Annual International Conference of the IEEE engineering in medicine and biology society*, pages 4729–4732. IEEE.

[de Armendi and Govindaraj, 2017] de Armendi, A. J. and Govindaraj, R. (2017). Pulse oximetry. *Data Interpretation in Anesthesia: A Clinical Guide*, pages 43–46.

[Dellacà et al., 2008] Dellacà, R. L., Zannin, E., Sancini, G., Rivolta, I., Leone, B. E., Pedotti, A., and Miserocchi, G. (2008). Changes in the mechanical properties of the respiratory system during the development of interstitial lung edema. *Respiratory research*, 9:1–9.

[Di Rienzo et al., 2011] Di Rienzo, M., Meriggi, P., Rizzo, F., Vaini, E., Faini, A., Merati, G., Parati, G., and Castiglioni, P. (2011). A wearable system for the seismocardiogram assessment in daily life conditions. In *2011 Annual International Conference of the IEEE Engineering in Medicine and Biology Society*, pages 4263–4266. IEEE.

[Elgendi, 2012] Elgendi, M. (2012). On the analysis of fingertip photoplethysmogram signals. *Current cardiology reviews*, 8(1):14–25.

[Engel et al., 2012] Engel, J. M., Mehta, V., Fogoros, R., and Chavan, A. (2012). Study of arrhythmia prevalence in nuvant mobile cardiac telemetry system patients. In *2012 annual International Conference of the IEEE engineering in medicine and biology Society*, pages 2440–2443. Ieee.

[Etemadi et al., 2015] Etemadi, M., Inan, O. T., Heller, J. A., Hersek, S., Klein, L., and Roy, S. (2015). A wearable patch to enable long-term monitoring of environmental, activity and hemodynamics variables. *IEEE transactions on biomedical circuits and systems*, 10(2):280–288.

[Fattah et al., 2017] Fattah, S. A., Rahman, M. M., Mustakin, N., Islam, M. T., Khan, A. I., and Shahnaz, C. (2017). Wrist-card: Ppg sensor based wrist wearable unit for low cost personalized cardio healthcare system. In *2017 IEEE Global Humanitarian Technology Conference (GHTC)*, pages 1–7. IEEE.

[Ganti et al., 2020] Ganti, V. G., Carek, A. M., Nevius, B. N., Heller, J. A., Etemadi, M., and Inan, O. T. (2020). Wearable cuff-less blood pressure estimation at home via pulse transit time. *IEEE Journal of Biomedical and Health Informatics*, 25(6):1926–1937.

[González et al., 2023] González, S., Hsieh, W.-T., and Chen, T. P.-C. (2023). A benchmark for machine-learning based non-invasive blood pressure estimation using photoplethysmogram. *Scientific Data*, 10(1):149.

[Gupta and Shea, 2021] Gupta, J. and Shea, M. (2021). Cardiovascular examination. *Merck Manual*. `https://www.merckmanuals.com/en-pr/professional/cardiovascular-disorders/approach-to-the-cardiac-patient/cardiovascular-examination`.

[Hernandez et al., 2014] Hernandez, J., Li, Y., Rehg, J. M., and Picard, R. W. (2014). Bioglass: Physiological parameter estimation using a head-mounted wearable device. In *2014 4th International Conference on Wireless Mobile Communication and Healthcare-Transforming Healthcare Through Innovations in Mobile and Wireless Technologies (MOBIHEALTH)*, pages 55–58. IEEE.

[Inan et al., 2018] Inan, O. T., Baran Pouyan, M., Javaid, A. Q., Dowling, S., Etemadi, M., Dorier, A., Heller, J. A., Bicen, A. O., Roy, S., De Marco, T., et al. (2018). Novel wearable seismocardiography and machine learning algorithms can assess clinical status of heart failure patients. *Circulation: Heart Failure*, 11(1):e004313.

[Inan et al., 2014] Inan, O. T., Migeotte, P.-F., Park, K.-S., Etemadi, M., Tavakolian, K., Casanella, R., Zanetti, J., Tank, J., Funtova, I., Prisk, G. K., et al. (2014). Ballistocardiography and seismocardiography: A review of recent advances. *IEEE journal of biomedical and health informatics*, 19(4):1414–1427.

[Kiranyaz et al., 2021] Kiranyaz, S., Avci, O., Abdeljaber, O., Ince, T., Gabbouj, M., and Inman, D. J. (2021). 1d convolutional neural networks and applications: A survey. *Mechanical systems and signal processing*, 151:107398.

[Lau et al., 2013] Lau, J. K., Lowres, N., Neubeck, L., Brieger, D. B., Sy, R. W., Galloway, C. D., Albert, D. E., and Freedman, S. B. (2013). iphone ecg application for community screening to detect silent atrial fibrillation: a novel technology to prevent stroke. *International journal of cardiology*, 165(1):193–194.

[Lee et al., 2013] Lee, J., Matsumura, K., Yamakoshi, K.-i., Rolfe, P., Tanaka, S., and Yamakoshi, T. (2013). Comparison between red, green and blue light reflection photoplethysmography for heart rate monitoring during motion. In *2013 35th annual international conference of the IEEE engineering in medicine and biology society (EMBC)*, pages 1724–1727. IEEE.

[Li et al., 2017] Li, S.-H., Lin, B.-S., Wang, C.-A., Yang, C.-T., and Lin, B.-S. (2017). Design of wearable and wireless multi-parameter monitoring system for evaluating cardiopulmonary function. *Medical Engineering & Physics*, 47:144–150.

[Liang et al., 2022] Liang, Y., Liu, G., Chen, Z., and Elgendi, M. (2022). PPG-BP Database.

[Maeda et al., 2011] Maeda, Y., Sekine, M., and Tamura, T. (2011). Relationship between measurement site and motion artifacts in wearable reflected photoplethysmography. *Journal of medical systems*, 35(5):969–976.

[McManus et al., 2013] McManus, D. D., Lee, J., Maitas, O., Esa, N., Pidikiti, R., Carlucci, A., Harrington, J., Mick, E., and Chon, K. H. (2013). A novel application for the detection of an irregular pulse using an iphone 4s in patients with atrial fibrillation. *Heart Rhythm*, 10(3):315–319.

[Menni et al., 2020] Menni, C., Valdes, A. M., Freidin, M. B., Sudre, C. H., Nguyen, L. H., Drew, D. A., Ganesh, S., Varsavsky, T., Cardoso, M. J., El-Sayed Moustafa, J. S., et al. (2020). Real-time tracking of self-reported symptoms to predict potential covid-19. *Nature medicine*, 26(7):1037–1040.

[Morillo et al., 2009] Morillo, D. S., Ojeda, J. L. R., Foix, L. F. C., and Jiménez, A. L. (2009). An accelerometer-based device for sleep apnea screening. *IEEE transactions on information technology in biomedicine*, 14(2):491–499.

[Odinaka et al., 2012] Odinaka, I., Lai, P.-H., Kaplan, A. D., O'Sullivan, J. A., Sirevaag, E. J., and Rohrbaugh, J. W. (2012). Ecg biometric recognition: A comparative analysis. *IEEE Transactions on Information Forensics and Security*, 7(6):1812–1824.

[Pandia et al., 2012] Pandia, K., Inan, O. T., Kovacs, G. T., and Giovangrandi, L. (2012). Extracting respiratory information from seismocardiogram signals acquired on the chest using a miniature accelerometer. *Physiological measurement*, 33(10):1643.

[Reali et al., 2022] Reali, P., Lolatto, R., Coelli, S., Tartaglia, G., and Bianchi, A. M. (2022). Information retrieval from photoplethysmographic sensors: A comprehensive comparison of practical interpolation and breath-extraction techniques at different sampling rates. *Sensors*, 22(4):1428.

[Salerno et al., 1992] Salerno, D. M., Zanetti, J. M., Poliac, L. C., Crow, R. S., Hannan, P. J., Wang, K., Goldenberg, I. F., and Van Tassel, R. A. (1992). Exercise seismocardiography for detection of coronary artery disease. *American journal of noninvasive cardiology*, 6(5):321–330.

[Sana et al., 2020] Sana, F., Isselbacher, E. M., Singh, J. P., Heist, E. K., Pathik, B., and Armoundas, A. A. (2020). Wearable devices for ambulatory cardiac monitoring: Jacc state-of-the-art review. *Journal of the American College of Cardiology*, 75(13):1582–1592.

[Semiz et al., 2020] Semiz, B., Carek, A. M., Johnson, J. C., Ahmad, S., Heller, J. A., Vicente, F. G., Caron, S., Hogue, C. W., Etemadi, M., and Inan, O. T. (2020). Non-invasive wearable patch utilizing seismocardiography for perioperative use in surgical patients. *IEEE Journal of Biomedical and Health Informatics*, 25(5):1572–1582.

[Shandhi et al., 2019] Shandhi, M. M. H., Semiz, B., Hersek, S., Goller, N., Ayazi, F., and Inan, O. T. (2019). Performance analysis of gyroscope and accelerometer sensors for seismocardiography-based wearable pre-ejection period estimation. *IEEE journal of biomedical and health informatics*, 23(6):2365–2374.

[Sohn et al., 2017] Sohn, K., Merchant, F. M., Sayadi, O., Puppala, D., Doddamani, R., Sahani, A., Singh, J. P., Heist, E. K., Isselbacher, E. M., and Armoundas, A. A. (2017). A novel point-of-care smartphone based system for monitoring the cardiac and respiratory systems. *Scientific reports*, 7(1):44946.

[Taebi et al., 2019] Taebi, A., Solar, B. E., Bomar, A. J., Sandler, R. H., and Mansy, H. A. (2019). Recent advances in seismocardiography. *Vibration*, 2(1):64–86.

[Tavakolian et al., 2012] Tavakolian, K., Portacio, G., Tamddondoust, N. R., Jahns, G., Ngai, B., Dumont, G. A., and Blaber, A. P. (2012). Myocardial contractility: A seismocardiography approach. In *2012 Annual International Conference of the IEEE Engineering in Medicine and Biology Society*, pages 3801–3804. IEEE.

[Van Houdt et al., 2020] Van Houdt, G., Mosquera, C., and Nápoles, G. (2020). A review on the long short-term memory model. *Artificial Intelligence Review*, 53:5929–5955.

[Wahlström et al., 2017] Wahlström, J., Skog, I., Händel, P., Khosrow-Khavar, F., Tavakolian, K., Stein, P. K., and Nehorai, A. (2017). A hidden markov model for seismocardiography. *IEEE Transactions on Biomedical Engineering*, 64(10):2361–2372.

[Walsh III et al., 2014] Walsh III, J. A., Topol, E. J., and Steinhubl, S. R. (2014). Novel wireless devices for cardiac monitoring. *Circulation*, 130(7):573–581.

[WHO, 2020] WHO (2020). The top 10 causes of death. *Geneva: World Health Organization*. `https://www.who.int/news-room/fact-sheets/detail/the-top-10-causes-of-death`.

[Wilson et al., 1993] Wilson, R. A., Bamrah, V. S., Lindsay Jr, J., Schwaiger, M., and Morganroth, J. (1993). Diagnostic accuracy of seismocardiography compared with electrocardiography for the anatomic and physiologic diagnosis of coronary artery disease during exercise testing. *The American journal of cardiology*, 71(7):536–545.

[Xing et al., 2023] Xing, D., Wang, Y., Sun, P., Huang, H., and Lin, E. (2023). A cnn-lstm-att hybrid model for classification and evaluation of growth status under drought and heat stress in chinese fir (cunninghamia lanceolata).

[Zakeri et al., 2016] Zakeri, V., Akhbardeh, A., Alamdari, N., Fazel-Rezai, R., Paukkunen, M., and Tavakolian, K. (2016). Analyzing seismocardiogram cycles to identify the respiratory phases. *IEEE Transactions on Biomedical Engineering*, 64(8):1786–1792.

[Zuckerman et al., 2016] Zuckerman, R. B., Sheingold, S. H., Orav, E. J., Ruhter, J., and Epstein, A. M. (2016). Readmissions, observation, and the hospital readmissions reduction program. *New England Journal of Medicine*, 374(16):1543–1551.

Appendix A

CIRCUIT SCHEMATICS OF THE PCBS

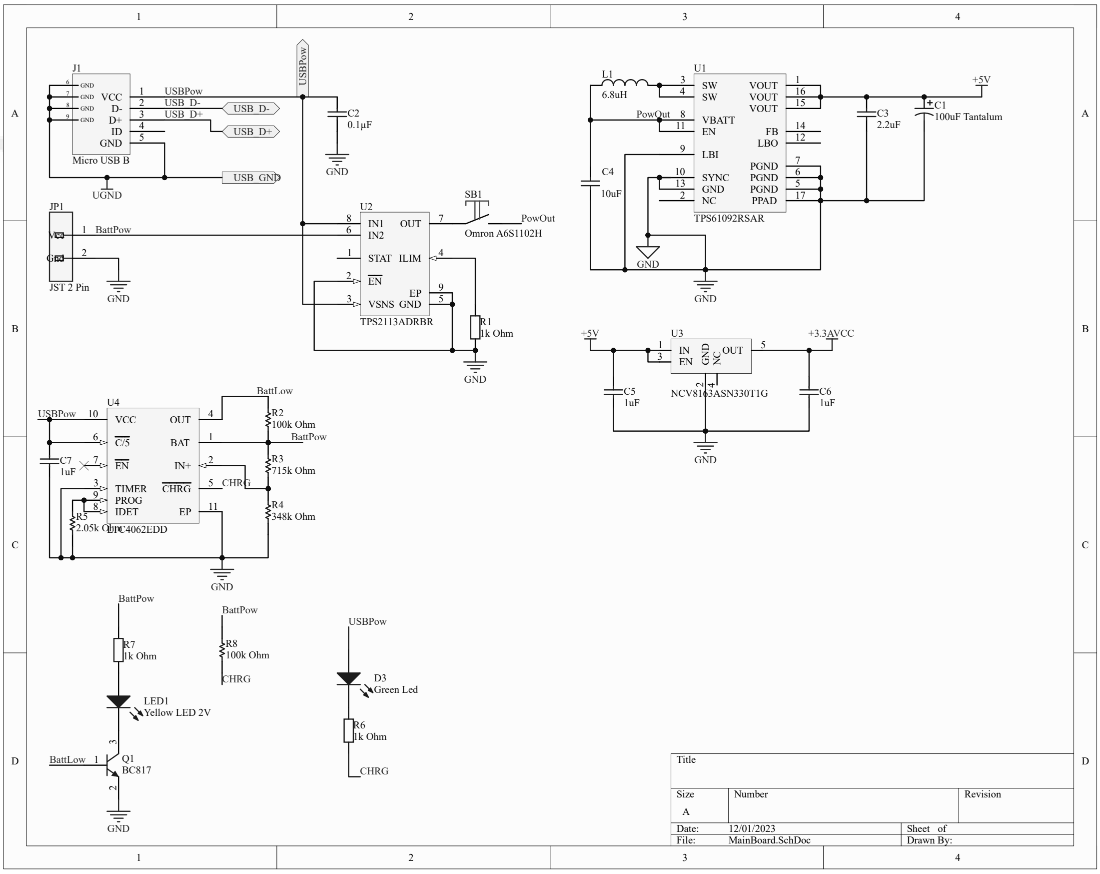

Figure A.1: Main Board Circuit Schematic #1.

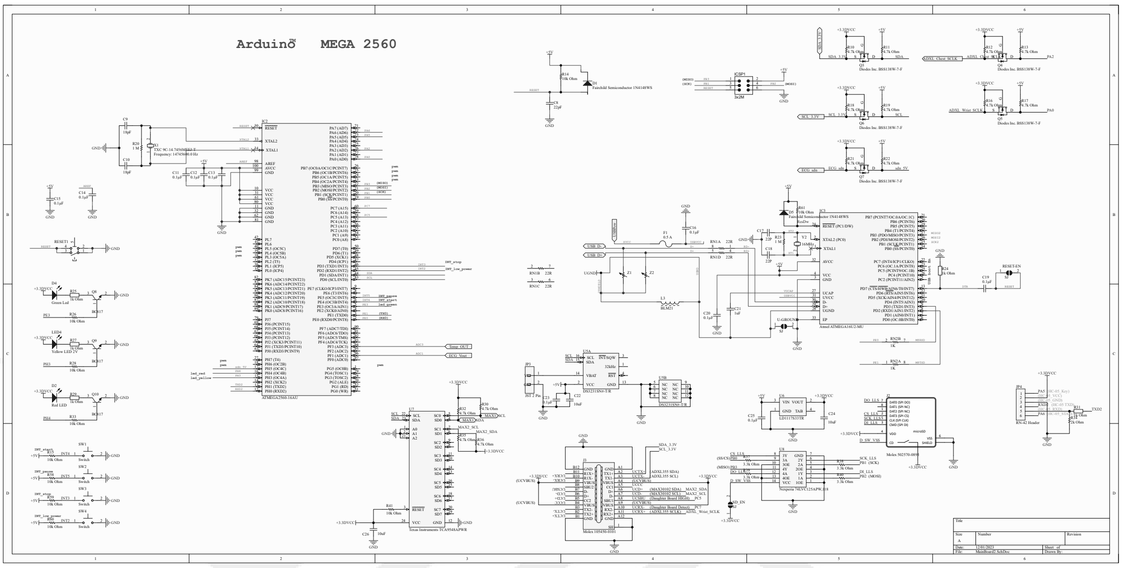

Figure A.2: Main Board Circuit Schematic #2.

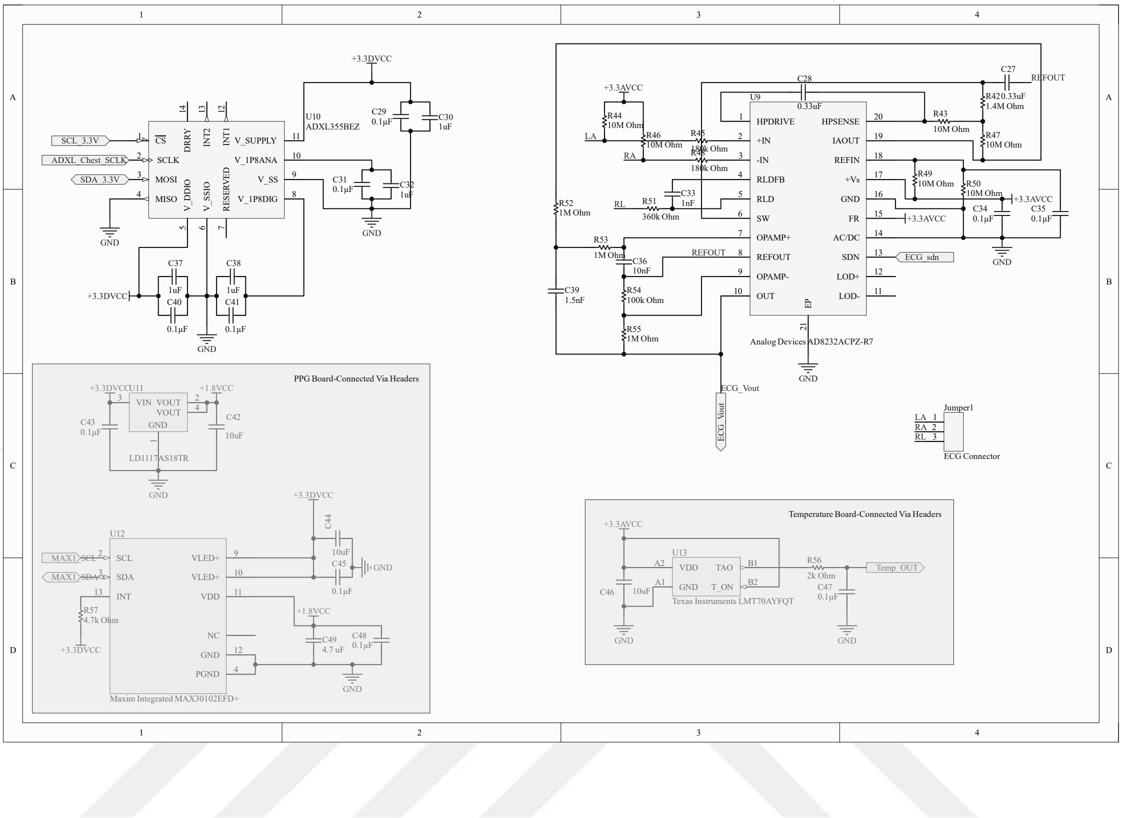

Figure A.3: Main Board Circuit Schematic #3.

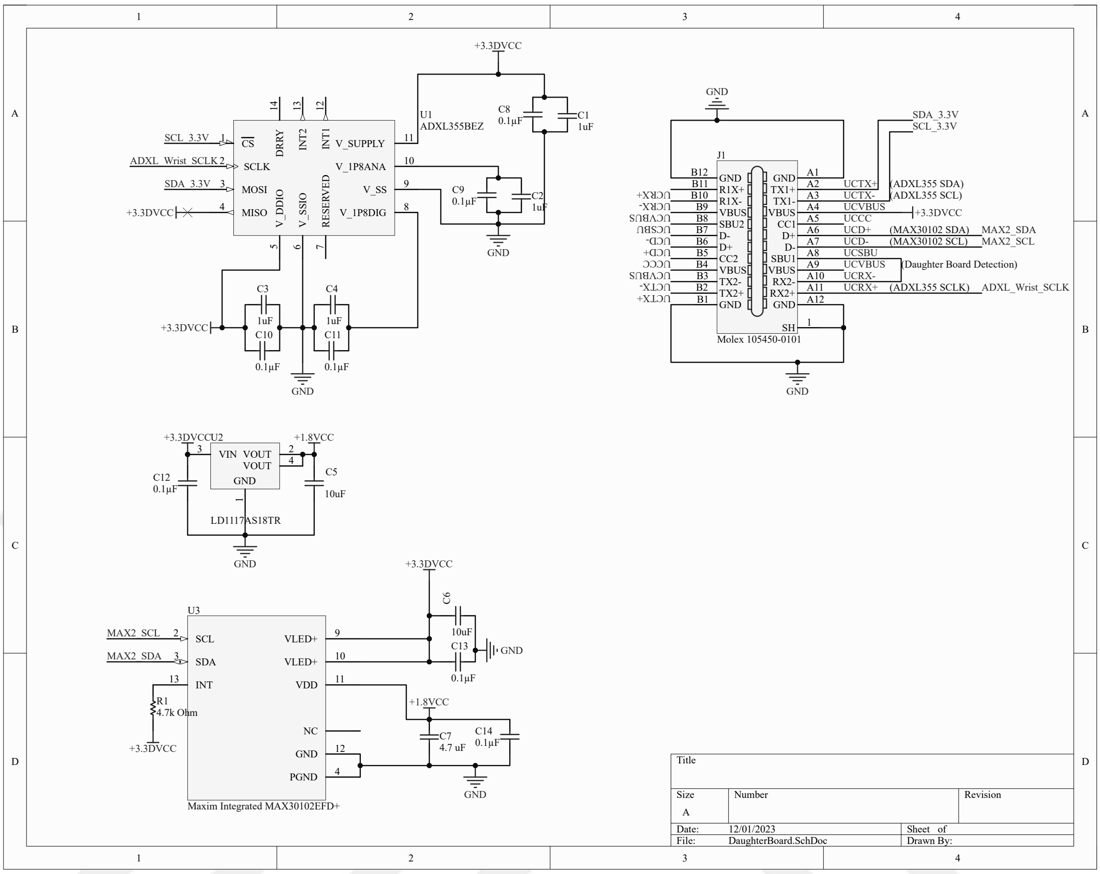

Figure A.4: Daughter Board Circuit Schematic.